

EXPERIMENTAL AND NUMERICAL INVESTIGATION OF
DAMAGE PROCESS IN COMPOSITE LAMINATES
UNDER LOW-VELOCITY IMPACT

A THESIS SUBMITTED TO
THE GRADUATE SCHOOL OF NATURAL AND APPLIED SCIENCES
OF
MIDDLE EAST TECHNICAL UNIVERSITY

BY

ÖMER TANAY TOPAÇ

IN PARTIAL FULFILLMENT OF THE REQUIREMENTS
FOR
THE DEGREE OF MASTER OF SCIENCE
IN
AEROSPACE ENGINEERING

FEBRUARY 2016

Approval of the thesis:

**EXPERIMENTAL AND NUMERICAL INVESTIGATION OF
DAMAGE PROCESS IN COMPOSITE LAMINATES
UNDER LOW-VELOCITY IMPACT**

submitted by **ÖMER TANAY TOPAÇ** in partial fulfillment of the requirements for the degree of **Master of Science in Aerospace Engineering Department, Middle East Technical University** by,

Prof. Dr. Gülbin Dural Ünver
Dean, Graduate School of **Natural and Applied Sciences**

Prof. Dr. Ozan Tekinalp
Head of Department, **Aerospace Engineering**

Assoc. Prof. Dr. Demirkan Çöker
Supervisor, **Dept. of Aerospace Engineering, METU**

Asst. Prof. Dr. Ercan Gürses
Co-Supervisor, **Dept. of Aerospace Engineering, METU**

Examining Committee Members

Prof. Dr. Orhan Yıldırım
Dept. of Mechanical Engineering, METU

Assoc. Prof. Dr. Demirkan Çöker
Dept. of Aerospace Engineering, METU

Prof. Dr. Altan Kayran
Dept. of Aerospace Engineering, METU

Prof. Dr. Mehmet Ali Güler
Dept. of Mechanical Engineering, TOBB ETU

Asst. Prof. Dr. Ercan Gürses
Dept. of Aerospace Engineering, METU

Date: 03.02.2016

I hereby declare that all information in this document has been obtained and presented in accordance with academic rules and ethical conduct. I also declare that, as required by these rules and conduct, I have fully cited and referenced all material and results that are not original to this work.

Name, Last name: Ömer Tanay Topaç

Signature:

ABSTRACT

EXPERIMENTAL AND NUMERICAL INVESTIGATION OF DAMAGE PROCESS IN COMPOSITE LAMINATES UNDER LOW-VELOCITY IMPACT

Topac, Omer Tanay

M.S., Department of Aerospace Engineering

Supervisor: Assoc. Prof. Dr. Demirkan Coker

Co-Supervisor: Asst. Prof. Dr. Ercan Gurses

February 2016, 77 pages

Damage sensitivity of composites under out-of-plane dynamic loading, and its limited detectability on a structure has long remained a prominent problem in industry. In this study, simulations are compared with the real-time damage formation scheme, with the aim of increasing confidence in failure predictions. Drop-weight impact experiments are carried out on a $[0/90]_5$ CFRP beam laminate. Initiation and progression of damage, consisting of matrix cracks and delamination, are visualized via ultra-high-speed camera at rates up to 60,000 fps and the sequence of failure events are captured. Evolution of dynamic strain fields is then quantified by a Digital Image Correlation (DIC) analysis and the resulting final failure patterns are characterized by a digital microscope. In the computational part, 3D finite element analysis is performed using ABAQUS/Explicit to simulate the experiments. Intraply matrix damage is modeled using a Continuum Damage Mechanics (CDM) based composite failure theory with LaRC04 initiation criterion and implemented via a user-written VUMAT subroutine. Delamination is modeled using cohesive interface elements introduced between $0^\circ/90^\circ$ interfaces. Damage initiation time, location and the interaction of failure modes and symmetry are compared with the experiments. The sequence of dynamic matrix cracking followed by dynamic delamination is observed for the first time. A good agreement between experimental and numerical results is achieved.

Keywords: composite materials, dynamic impact, matrix failure, delamination, experimental validation.

ÖZ

KOMPOZİT LAMİNATLARDA DÜŞÜK HIZLI DARBE SONUCU OLUŞAN HASARIN DENEYSEL VE HESAPLAMALI OLARAK İNCELENMESİ

Topaç, Ömer Tanay

Yüksek Lisans, Havacılık ve Uzay Mühendisliği

Tez Yöneticisi: Doç. Dr. Demirkan Çöker

Ortak Tez Yöneticisi: Yard. Doç Dr. Ercan Gurses

Şubat 2016, 77 sayfa

Kompozit malzemelerin düzleme dik yönde gelen dinamik yükleme altında hasar oluşum hassasiyeti ve bu hasarın yapıda tespitinin zorluğu endüstrinin ciddi bir sorunu olarak süregelmiştir. Bu çalışmada, hasar öngörülerine olan güveni artırmak amacıyla hesaplamalı simülasyonlar gerçek hasar oluşum mekanizmasıyla karşılaştırılmıştır. $[0/90]_s$ dizimli kiriş laminatlara serbest düşüş darbe deneyleri gerçekleştirilmiştir. Matris çatlağı ve delaminasyondan oluşan hasarın başlangıcı ve ilerlemesi 60,000 kare/saniye hızında gözlemlenerek hasar oluşum sırası kaydedilmiştir. Ardından, dinamik gerinim alanlarının gelişimi Dijital Resim Korelasyonu (DIC) yöntemiyle sayısallaştırılmış ve sonuçta meydana gelen hasar dijital mikroskop ile karakterize edilmiştir. Hesaplamalı kısımda, deneyler 3 boyutlu modellenerek ABAQUS/Explicit sonlu eleman yazılımında ile simüle edilmiştir. Lamina içi matris hasarı sürekli hasar mekaniği (CDM) temelli, LaRC04 hasar oluşum kriterini içeren, bir VUMAT altprogramı ile simülasyonlara entegre edilmiştir. Delaminasyon ise $0^\circ/90^\circ$ lamina aralarına eklenen kohesif arayüz elemanları ile modellenmiştir. Hasar oluşum zamanı, yeri ve hasar modlarının birbirleriyle etkileşimi deneylerle karşılaştırılmıştır. Darbe altında dinamik matris hasar oluşumu ve delaminasyonla etkileşimi ilk kez gözlemlenmiştir. Genel olarak deneyler ve simülasyonlar arasında iyi bir uyum elde edilmiştir.

Anahtar Kelimeler: kompozit malzemeler, dinamik darbe, matris hasarı, delaminasyon, deneysel geçерleme

*To my love Begüm—
the one who has always been with me,
and to my parents Belkis and Önder—
those who have chosen to put up with me*

ACKNOWLEDGEMENTS

First and foremost, I would like to present my sincere gratitudes to my advisors Dr. Demirkan Çöker and Dr. Ercan Gürses. This thesis could not be possible without the incomparable support of Dr. Cöker in the most desperate times and his everlasting confidence in me. More than anything else, he has been a mentor to me with his tireless pursuit of perfection that has reshaped my life perception. Guidance of Dr. Gürses have tremendously evolved this study and led me to focus on what is important. This thesis could never be in its current maturity without his unifying and completing touches.

I would like to thank my first and former leader at TAI, Dr. Burak Gözlüklü, whose encouragement pave the way for this thesis. His priceless recommendations made this study an original work of literature. I would also like to express my appreciation to my love Begüm Erdem for her all along mental and physical assistance with a never-ending faith in me.

I would like to thank Dr. Orhan Yıldırım, Dr. Altan Kayran and Dr. Mehmet Ali Güler for attending my thesis defense presentation with their valuable comments. I would also like to thank Turkish Aerospace Industries for generously supporting my graduate studies while I have been working in full-time.

I would like to thank fellow students at our lab, Ali Gezer, Burcu Taşdemir, Miray Aydan Arca and İmren Uyar for their assistance throughout the study. Last but not least, I would like to thank METU Center for Wind Energy (METUWIND) for granting access to their experimental facilities.

TABLE OF CONTENTS

ABSTRACT.....	v
ÖZ.....	vi
ACKNOWLEDGEMENTS.....	ix
TABLE OF CONTENTS.....	x
LIST OF TABLES.....	xii
LIST OF FIGURES.....	xiii
LIST OF ABBREVIATIONS.....	xvi
LIST OF SYMBOLS.....	xvii
CHAPTERS	
1. INTRODUCTION.....	1
1.1. Composite Material Usage.....	1
1.2. Out-of-Plane Low-Velocity Impact.....	2
1.3. Investigation of Impact-Induced Damage of Composites.....	3
1.3.1. Experimental Studies.....	3
1.3.2. Numerical Studies.....	4
1.4. Mechanism Based Damage Models.....	6
1.5. Scope of This Study.....	6
2. EXPERIMENTAL METHOD.....	9
2.1. Specimen Preparation.....	9
2.2. Test Procedure.....	10

2.3.	Digital Image Correlation (DIC).....	11
3.	NUMERICAL METHOD.....	13
3.1.	Intralaminar Damage Model.....	14
3.1.1.	Damage Initiation Criterion.....	15
3.1.2.	Damage Evolution Criterion.....	17
3.1.3.	Stiffness Degradation Scheme.....	19
3.2.	Interlaminar Damage Model.....	19
3.3.	Simulations of Impact Experiments.....	22
4.	EXPERIMENTAL RESULTS.....	25
4.1.	Failure Mechanism.....	26
4.2.	Micro-matrix Cracks.....	28
5.	NUMERICAL RESULTS.....	31
5.1.	Failure Progression Sequence.....	31
5.2.	Failure Mechanism.....	34
5.3.	Global Response.....	36
5.4.	Full-Scale Model vs. Symmetric-Half Model.....	38
5.5.	Effect of Mesh Symmetry.....	41
6.	DISCUSSION.....	47
6.1.	Effect of Matrix Failure Properties on Failure Initiation, Angle and Time.....	54
7.	CONCLUSIONS.....	57
	REFERENCES.....	59
	APPENDIX.....	65

LIST OF TABLES

TABLES

Table 1: Interface properties of Hexcel 913C/HTS material.....	21
Table 2: Mechanical properties of Hexcel 913C/HTS material.....	23
Table 3: Matrix cracking sequence, angle, location and time of 6 test specimens....	26

LIST OF FIGURES

FIGURES

Figure 1: Internal damage resulting from tool drop.....	2
Figure 2: Impact damage induced by (a) interlaminar shear and (b) bending stresses [18].....	3
Figure 3: Two-dimensional impact proposed by Choi et al. [5] and resulting damage pattern.	4
Figure 4: ASTM D7136 standard test setup.....	4
Figure 5: Matrix failure and delamination pattern predicted by simulations of Lopes et al. [24].....	5
Figure 6: (Left) An unpainted specimen used in the experiments and (right) its section view captured by the microscope.....	9
Figure 7: (a) Architectural design of the experimental setup and (b) photograph of the actual experimental setup.....	11
Figure 8: Stochastic paint of DIC on a specimen, strain computation zone and representative facet mesh.....	11
Figure 9: (a) Computational model and (b) a representative section of the (left) regular and (right) fine mesh.....	14
Figure 10: Constitutive response of interlaminar damage model.....	14
Figure 11: Saturation type evolution behavior of matrix damage variable d	18
Figure 12: Bi-linear traction-separation response of the interlaminar damage model.....	20
Figure 13: Mixed-mode response of interlaminar cohesive zone model (CZM).....	20
Figure 14: Micrograph images of visible central regions of damaged mid-layer of specimens.....	25
Figure 15: High-speed camera images showing (a) the impactor and specimen just before impact and enlarged view of (b) intact specimen, (c) initiation of matrix cracking and (d) propagation of damage to delamination.	27
Figure 16: Typical damage initiation and propagation sequence of (a) first and (b) second crack.....	28

Figure 17: Major strain fields showing (top) no directionality at 266 μ s, (middle) diagonal directionality just before the first crack at 317 μ s and (bottom) after the first crack.....	29
Figure 18: Micro matrix cracks observed in the neighborhood of upper interface. ..	29
Figure 19: (Top) Upper interface of specimen 5, (Left) showing debris formation during delamination and (Right) semi-intact regions near impact center.....	30
Figure 20: Three-dimensional damage initiation and propagation sequence and resulting failure pattern.	32
Figure 21: Matrix failure and delamination schemes when damage is completely propagated in (a) regular mesh and (b) fine mesh model.	34
Figure 22: The path where matrix failure criterion is captured (white line).....	34
Figure 23: Evolution of tensile matrix failure criterion for regular mesh (dashed lines) and fine mesh (solid lines).....	35
Figure 24: Load vs. Displacement responses of regular and fine mesh models.	36
Figure 25: Evolution of energy parameters in the system with time, starting from the impact instance.....	37
Figure 26: Symmetric-half model used in the simulations.	38
Figure 27: Final matrix failure and delamination schemes in regular meshed (a) symmetric-half and (b) full-scale models.	39
Figure 28: Evolution of tensile matrix failure criterion in the regular meshed symmetric-half (bold lines) and full-scale (light lines) models.	40
Figure 29: Load vs. Displacement responses of symmetric-half and full-scale models.	41
Figure 30: Five different mesh patterns of the beam and impactor positioning above the beam. (a) regular mesh with impactor placed above a node, (b) regular mesh with the impactor placed above an element, (c) unsymmetric mesh with larger elements just under the impactor, (d) unsymmetric mesh with two distinct mesh size and (e) unsymmetric mesh with diagonal elements.	42
Figure 31: Matrix failure in the models given in Figure 30 at their failure initiation instances.....	43
Figure 32: Matrix failure in the models given in Figure 30, once damage is almost completely propagated, 20 μ s later than corresponding damage initiation.....	45

Figure 33: Transverse engineering shear strain (γ_{yz}) contours of (a) DIC analysis, (b) FE analysis just before crack initiation and (c) just after crack initiation.	48
Figure 34: Transverse engineering shear strain evolution (γ_{23}) along the centerline in experiments and simulations.....	49
Figure 35: Evolution of transverse shear strain (γ_{23}) along the centerline with 16 μ s interframe time in (a) experiments and (b) analysis.	51
Figure 36: Evolution of shear strain obtained from DIC and FEM at the point A shown in Figure 33.....	52
Figure 37: Matrix failure initiation and delamination propagation obtained from simulations (left) and experiments (right).....	53
Figure 38: Delamination footprint of experimental average and prediction of FE analysis.....	54
Figure 39: Damage initiation locations; (top) observed in six specimens and (bottom) obtained from simulations with 2% weaker and 2% stronger material properties, with initiation times. Results are normalized at the left side.	55

LIST OF ABBREVIATIONS

ASTM	American Society for Testing and Materials
BVID	Barely Visible Impact Damage
CDM	Continuum Damage Mechanics
CFRP	Carbon-Fiber-Reinforced Polymer
CZM	Cohesive Zone Method
DIC	Digital Image Correlation
FPS	Frames per Second
LVI	Low-Velocity Impact
SAE	Society of Automotive Engineers
UMAT	Material Subroutine for ABAQUS/Standard
VUMAT	Material Subroutine for ABAQUS/Explicit
WWFE	World-Wide Failure Exercise

LIST OF SYMBOLS

$\langle \rangle$	Macaulay bracket
C	Stiffness matrix
d_m	Damage variable of matrix material
d_s	Damage variable of shear factor
E_0	Penalty stiffness
E_{ij}	Elastic modulus tensor
g	Toughness ratio for LaRC04 criterion
G_C	Fracture toughness
G_{iC}	Critical energy release rate under Mode- i loading
G_{ij}	Shear modulus tensor
l	Deformed vertical and horizontal component of length
l_0	Undeformed vertical and horizontal component of length
L^C	Characteristic element length
S	Compliance matrix
S_{is}^L	In-situ longitudinal shear strength
S^L	Longitudinal shear strength
S^T	Transverse shear strength
t	Thickness
T	Traction stresses in cohesive elements
T_{max}	Maximum traction attained during loading of a cohesive element
$T_{o,i}$	Pure mode interfacial normal and shear strength tensor
Y_{is}^T	In-situ transverse tensile strength
Y^T	Transverse tensile strength
α	Angle of fracture plane forming with vertical
α_0	Common value of 53° for α
$\gamma_{12 is}^u$	In-situ in-plane ultimate strain
γ_{ij}	Engineering shear strain tensor
δ	Separation distance of cohesive elements
$\delta_{c,i}$	Pure mode critical displacement tensor

δ_{eq}^0	Equivalent displacement at the initiation instance of damage
δ_{eq}^f	Equivalent displacement of completely propagated damage
δ_{eq}	Equivalent displacement
$\delta_{o,i}$	Pure mode onset of separation tensor
ϵ_e	Engineering strain
ϵ_{ij}	Strain tensor
ϵ_t	True strain
η	B-K criterion constant
η^L	Friction coefficient in a ply in longitudinal direction
η^T	Friction coefficient in a ply in transverse direction
Λ^o	Crack tensor proposed by Laws [42]
ν_{ij}	Poisson's ratio
σ_{eq}	Equivalent stress
σ_{ij}	Stress tensor
σ_n	Normal stress component acting on the fracture plane
τ^L	Longitudinal stress component acting on the fracture plane
τ^T	Transverse stress component acting on the fracture plane
$x(\gamma_{12})$	Integration of the in-plane shear stress-strain curve

CHAPTER 1

INTRODUCTION

In this chapter the composite applications and the critical loading conditions that pose a safety concern for composite materials are described. Then, out-of-plane low-velocity impact that composite structures undergo during their operation life is described, with the corresponding safety concerns it poses. Next, common experimental approaches for understanding the damage mechanism under low-velocity impact and recent computational efforts for improving the conventional approaches are detailed. Later, mechanism based computational damage models and related experimental work are given. Finally, the scope of current study is briefly outlined.

1.1. Composite Material Usage

As a general term, composite materials are defined as new materials formed from the combination of two existing materials to exploit advantages of both. By definition, composite materials have a broad scope ranging from rehabilitation applications in civil engineering to many light-weight products. This thesis focuses on the behavior of Carbon-fiber-reinforced polymer (CFRP) composites that are mostly used in aerospace applications.

Increased usage of CFRP composites allows the most efficient products ever built [1]. Composite materials are more commonly preferred in weight-critical applications mainly because of their superior specific strength properties. The ratio of strength per weight is termed as specific strength, and this ratio is up to five times greater in carbon-epoxy composites than in aluminum alloys [2]. Other benefits of composites include more efficient manufacturability for curved profiles, increased fatigue life and corrosion resistance [3].

Nevertheless, orthotropic composition of composites and brittle behavior of carbon material create a major damage sensitivity risk if the structure is loaded in weaker transverse direction, where load is carried by matrix material. Such characteristic gets

even more significant in safety and reliability critical aerospace applications under dynamic loading that doubles the effective stresses. Transverse dynamic loading generally takes place as impact by foreign objects. This phenomenon has been extensively studied in the literature in terms of understanding the damage mechanism [4–6], the effects of geometry [7–10] and the impact parameters [11–13] for improving damage resistance of structures.

1.2. Out-of-Plane Low-Velocity Impact

Impacts occurring at speeds 1 to 10 m/s are usually produced by accidental stepping, hail storm and tool drops, and are classified as low-velocity impact (LVI) by Cantwell and Morton [14]. LVI often creates damage with dent depths lower than barely visible impact damage (BVID) threshold [15] as illustrated in Figure 1; thus it can be overlooked easily by standard inspections. However, the damage consisting of matrix failure and delamination may significantly reduce the residual strength of the structure, particularly under compressive loading [16]. Because of this phenomenon, composite structures are assumed to contain an internal damage in the design phase [15], adding extra weight burden.

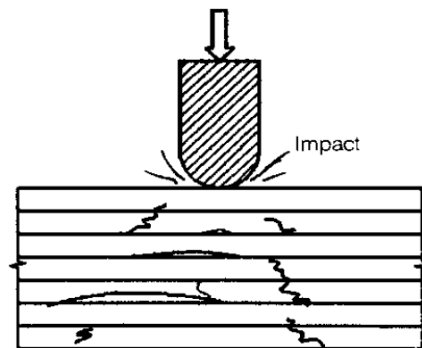


Figure 1: Internal damage resulting from tool drop.

Under low-velocity impact loading, several physical parameters affect the damage mechanisms of unidirectional laminated composites [14]. Matrix cracks are usually triggered as the initial failure mode due to interlaminar shear or bending stresses [17] as represented in Figure 2. As the secondary damage mode, delamination is generated by the progression of matrix cracks towards the ply interfaces with different fiber orientations, due to stiffness mismatch at the interface [6].

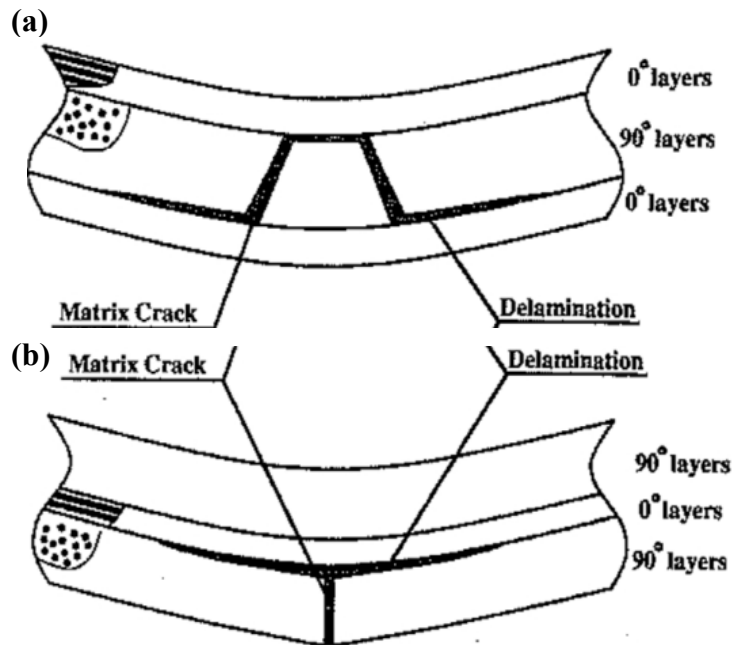


Figure 2: Impact damage induced by (a) interlaminar shear and (b) bending stresses [18].

1.3. Investigation of Impact-Induced Damage of Composites

Damage occurring in composite laminates under impact is thoroughly investigated in literature. Among these studies, more conventional approaches mostly consist of experimental work, whereas more recent work is focused on damage predictions by numerical simulations.

1.3.1. Experimental Studies

Most of the early experimental work in composite impact is focused on understanding the damage mechanisms. To identify complex mechanisms, *model* experiments have long been used to reveal the underlying basic physics by simplifying the process. For LVI, model experiments were usually conducted on coupon level simplified stacking sequence laminates to form distinct failure modes. Richardson and Wisheart [19] have made a comprehensive review consisting of these studies. One of the pioneering studies are performed by Choi and his co-workers [5]. The authors proposed a line-loading approach through the width of a specimen, which allowed an easier non-destructive visualization of damage from the sides and simplified the impact event to almost a two-dimensional setting. According to the post-mortem characterization of damage, the authors claimed that the failure initiates as two symmetric shear matrix cracks, followed by delamination with many micro-matrix cracks, as illustrated in Figure 3.

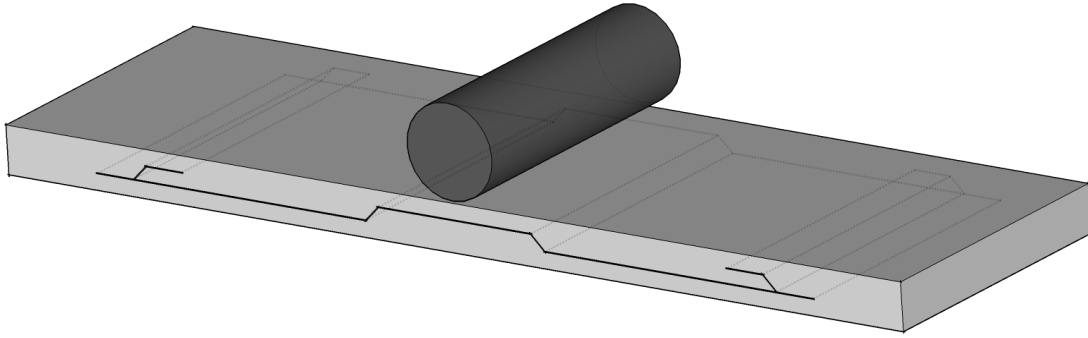


Figure 3: Two-dimensional impact proposed by Choi et al. [5] and resulting damage pattern.

More recently, ASTM has proposed a test method for determination of impact resistance of composites with D7136 standard [20] as illustrated in Figure 4. In this method, a plate geometry specimen is loaded by a point impactor at its center and the boundary condition effects are minimized by the support structure placed at the bottom. Upon tests, impact resistance of the material is quantified by the force-displacement history and the resulting delamination size. ASTM has also suggested a sequential test method for measuring the residual compressive strength of the structure through D7137 standard [21].

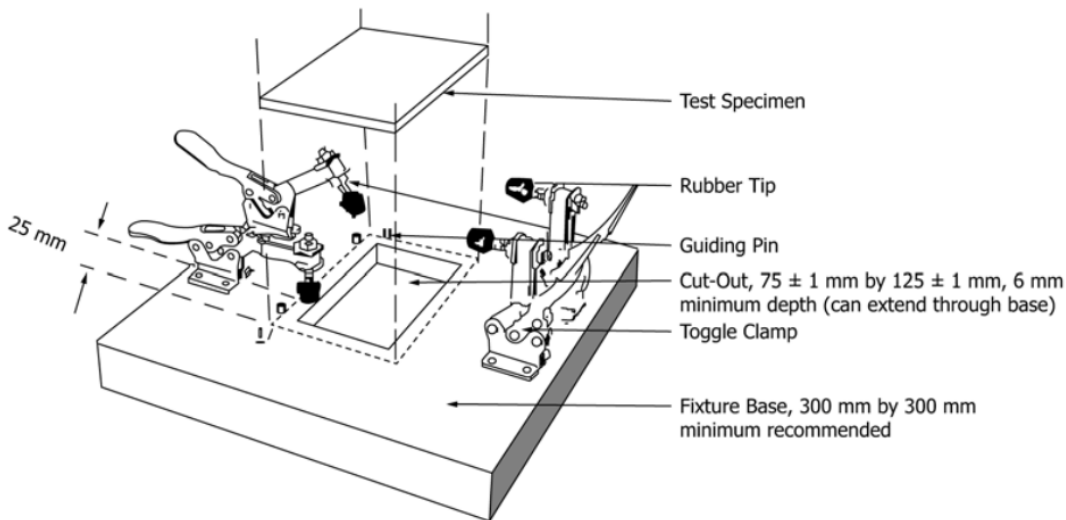


Figure 4: ASTM D7136 standard test setup

1.3.2. Numerical Studies

In the literature, modeling of impact-induced damage of composite laminates has been studied through different approaches, mostly at the meso-scale. Geubelle and Baylor

[22] have conducted one of the first computational efforts by simulating the pioneering work of Choi et al. [5]. In that study, the final failure pattern of the experiments is successfully predicted with a symmetric 2D computational model by using cohesive elements for the simulation of both matrix cracking and delamination.

Simulating ASTM D7136 impact test [20] with finite element method has recently gained significant attention. The ultimate goal is to develop predictive numerical methods that will decrease the required number of tests for certification [23].

One of the recent works in this scope has been conducted by Lopes et al. [24] in the investigation of the effects of dispersed stacking sequence. In this study, most recent damage modeling and simulation approaches have been attained. Ply damage is modeled by a 3D Continuum Damage Mechanics (CDM) based theory with LaRC04 initiation criterion [25,26] and an improved cohesive element formulation [27] for delamination. After the simulations a complex 3D damage pattern is obtained as given in Figure 5.

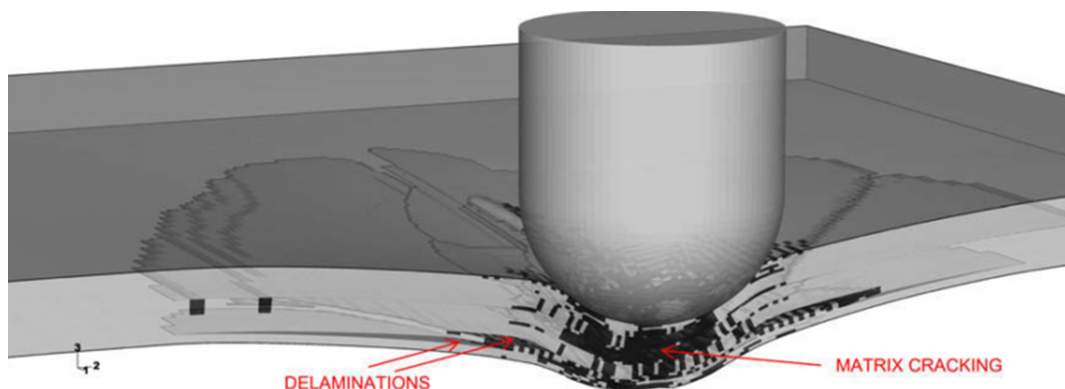


Figure 5: Matrix failure and delamination pattern predicted by simulations of Lopes et al. [24].

In a similar numerical study, Shi et al. [28] inserted cohesive elements at predetermined transverse matrix crack locations to simulate splitting failure within a ply. It was stated that the use of cohesive elements in addition to a 2D ply failure criterion resulted in a better correlation of experiments. Bouvet et al. [29], utilized zero-volume spring elements at the finite element boundaries for modeling both matrix damage and delamination. Later, Bouvet et al. [30] further extended their spring model to capture permanent indentation caused by low-velocity impact.

Although, a considerable number of approaches have been developed for the modeling of damage in composites, the comparisons of these models with experiments were limited to post-mortem damage footprints and global load responses. To this end, validation of these models in terms of the initiation and evolution process of damage is still lacking.

1.4. Mechanism Based Damage Models

Mechanism based damage models were first recognized by Puck and Schürmann in the early 2000's [31] for explicitly modeling the fiber and matrix failure instead of ply-based failure models such as Tsai-Wu method [32]. Recently, Talreja [33] emphasized that the accuracy of failure models critically depends on the correct simulation of the damage mechanism.

Despite the significance of these methods, there are very few experimental studies in literature that aims to capture the damage process to correlate these computational methods with experiments. In the early 80's Takeda et al. [34] used a high-speed camera to observe the evolution sequence of matrix cracking and delamination damage on a glass-fiber composite under ballistic impact. More recently, Xu and Rosakis [35] investigated the damage process of two layer heterogeneous materials under low-velocity impact.

1.5. Scope of This Study

Understanding the failure sequence in composites paves the way for the development of better computational methods and hence it is of utmost importance. The goal of this study is to elucidate the complex failure process of composites subjected to low-velocity impact by using a combined experimental and numerical approach. To this end, simplified line-load impact experiments are conducted on a clamped $[0_5/90_3]_s$ CFRP beam laminate. During the experiments, damage initiation and evolution processes are captured by a high-speed camera at up to 60,000 frames per second (fps) in conjunction with Digital Image Correlation (DIC) analysis to generate dynamic full-field strain contours. Following the experiments, the characteristics of failure are studied in detail by microscopy of post-mortem specimens. On the computational side, FE simulations are conducted in ABAQUS/Explicit. Intraply matrix cracking is considered in a 3D Continuum Damage Mechanics (CDM) framework by implementing LaRC04 [25] failure initiation criterion into a user-written VUMAT

subroutine. Delamination is simulated by using cohesive interface elements with the traction-separation response proposed by Camanho and Dávilla [36].

The thesis is structured as follows: In the following section, impact test setup and experimental procedure are described. In the third section, the numerical method is presented with brief descriptions of ply damage and delamination models. In the fourth section, the experimental observations and computational results of finite element analyses are presented. In the fifth section, the results of experiments and simulations are comparatively discussed in terms of damage initiation time, propagation sequence and sensitivity to parameters. Finally, the conclusions are presented in the sixth section, with possible future studies.

CHAPTER 2

EXPERIMENTAL METHOD

In the experimental part of this study, a set of non-standard drop-weight impact tests is carried out on CFRP beam laminates. The main objective of these experiments is to visualize the time-dependent damage evolution process during the impact event. The stacking is chosen as $[0_5/90_3]_s$ in order to achieve distinct damage modes and clear visualization by having thick clustered plies with an angle variation of 90 degrees.

2.1. Specimen Preparation

A plate is manufactured from Hexcel 913C-HTS carbon-epoxy unidirectional preregs by hand lay-up technique. Following the standard curing process, the plate is scanned with ultrasonic (C-Scan) inspection to eliminate unacceptable manufacture defects. The plate is then cut by a diamond cutter into 100 mm X 17 mm beams with 4.8 mm thickness and holes are drilled at both edges of the beams. Edge section of each specimen is polished to provide better visualization and scanned with Huvitz HDS-SS50 optical microscope to eliminate any defects induced by the processes. Close-up photo of a finalized specimen is presented in Figure 6. Second set of specimens, which are used in DIC analysis, is painted with a stochastic pattern composed of black dots on a white background. On the other hand, the impactor is made of SAE 304 steel material as rectangular prism geometry, having a cylindrical head of 40mm diameter. The width of impactor matched that of the specimen to create uniform line-loading impact, resulting a total weight of 0.785kg.

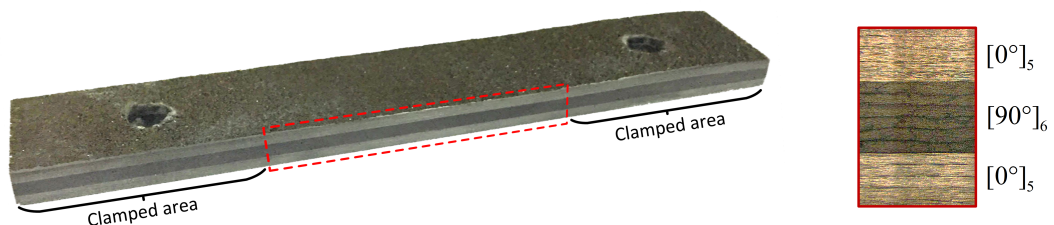
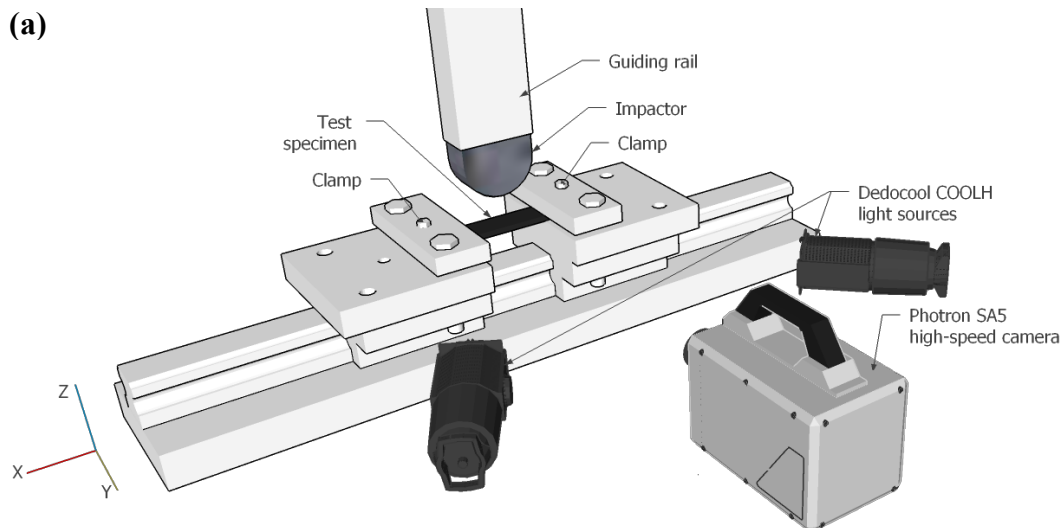


Figure 6: (Left) An unpainted specimen used in the experiments and (right) its section view captured by the microscope.

2.2. Test Procedure

A line-load impact fixture, similar to the one proposed by Choi et al. [5], is designed as shown in Figure 7a. The experiment design allows capturing side section of the specimen during the tests. The specimen is clamped to the fixture by means of grips squeezing the 25mm portion of each end from upper and lower faces. Furthermore, screws are placed in the drilled holes of the specimen to prevent in-plane slippage under impact. In experiments, a millimetric scale is taped to the bottom of the specimen for accurate measurement. The impactor is dropped through a guiding rail from 1 m height, theoretically creating 7.7 J of impact energy and 4.3 m/s velocity just before impact. This speed is also confirmed by high-speed camera pictures, indicating that the friction in the guiding rail is negligible. The rebound of the impactor after the first impact is prevented to avoid the formation of any additional damage.

During tests, the specimen is illuminated via two Dedocol COOLH light systems equipped with 250W Osram HLX Tungsten lamps. The impact event is captured in 2D via one Photron SA5 ultra-high speed camera from the side section of specimens at 60,000 frames per second (fps). Shutter speed is set to highest possible with available lighting to have dynamic images as sharp as possible. Upon each experiment, matrix cracking and delamination damage in specimens are characterized by Huvitz HDS-SS50 microscope at 50x, 140x and 200x magnification levels.



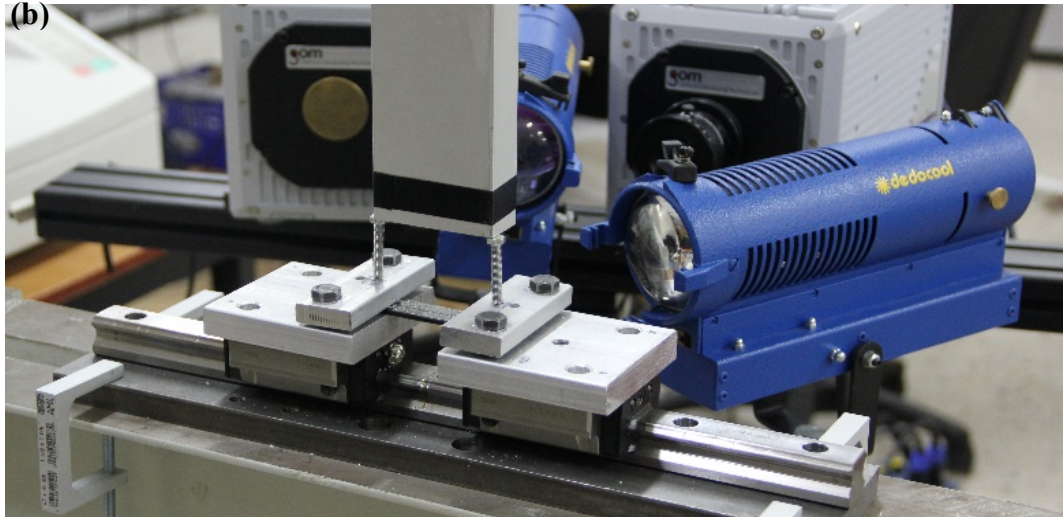


Figure 7: (a) Architectural design of the experimental setup and (b) photograph of the actual experimental setup.

2.3. Digital Image Correlation (DIC)

In this study, DIC analysis is performed for two purposes; correlating strain history during elastic loading stage and capturing initiation of matrix damage. Two-dimensional DIC is performed on images taken from the high-speed camera at 60,000 fps. Evolution of displacement and strain fields are measured at the painted surfaces of the beam specimens in ARAMIS software. The computations are made at many subsets defined as facets, each capturing the change in stochastic pattern between subsequent images. In calculations, facet size is chosen as 14 pixels in accordance with the resolution of stochastic pattern with 7 pixels overlapping each other for better accuracy. DIC evaluation area in a specimen and a representative facet mesh are given in Figure 8.

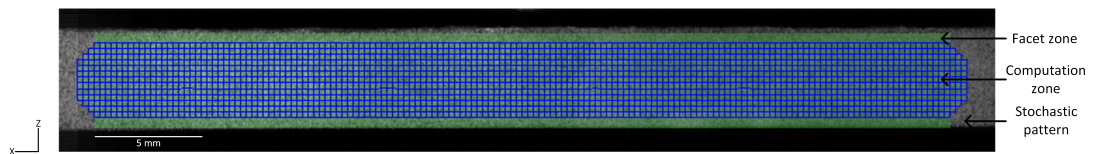


Figure 8: Stochastic paint of DIC on a specimen, strain computation zone and representative facet mesh.

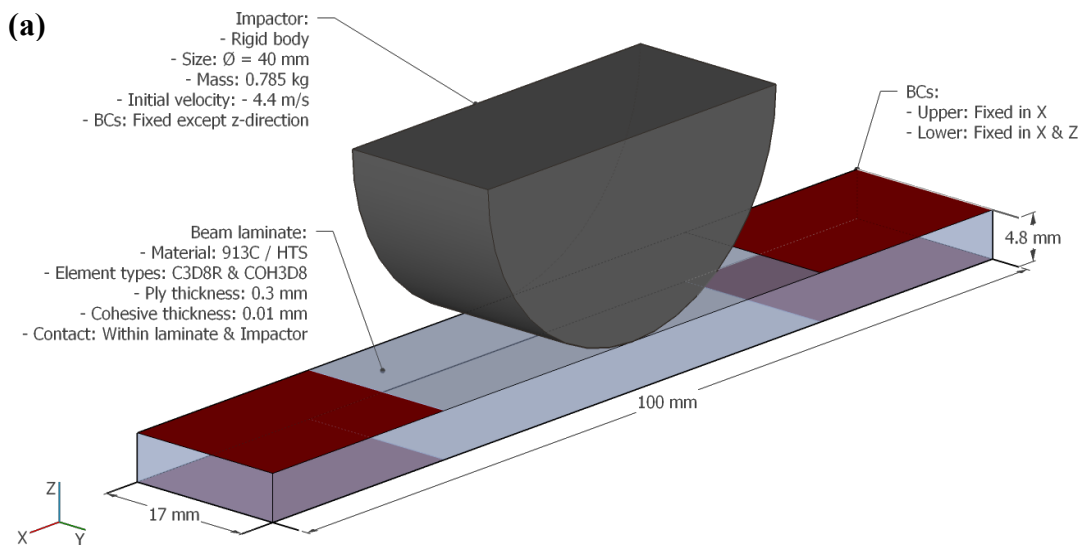
Vertical and horizontal components of displacement increments are calculated for each facet and then converted to engineering strain of horizontal and vertical components by using $\epsilon_e = (l - l_0)/l_0$. Scaling this definition down to each facet point, horizontal

and vertical components of strain become $\epsilon_x = \frac{\partial u}{\partial x}$ and $\epsilon_y = \frac{\partial v}{\partial y}$. Similarly, shear component of engineering strain is calculated as $\gamma_{xy} = \frac{\partial v}{\partial x} + \frac{\partial u}{\partial y}$. However, in the current case of finite deformations, true strains are required. Engineering strains are converted to true strains according to $\epsilon_t = \ln(\epsilon_n + 1)$. Using true strain values for each facet overall strain field in entire surface is derived.

CHAPTER 3

NUMERICAL METHOD

In this section, the numerical approach employed in the simulations is presented. The main objective of finite element analyses is to simulate the failure process occurring in the experiments in a realistic manner. Therefore, the computational models are built with the aim of representing the test conditions as closely as possible. Although the impact case can be idealized as 2D plane strain, the computational modeling is done in a 3D environment to include the three-dimensional effects. Simulations are conducted in ABAQUS/Explicit as represented in Figure 9a. The geometries are discretized by regular mesh and fine mesh patterns as represented in Figure 9b. In all three models, intralaminar ply damage in middle 90° layer and interlaminar delamination damage in cohesive layers are considered.



(b)

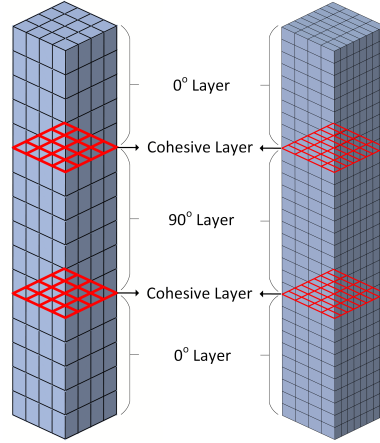


Figure 9: (a) Computational model and (b) a representative section of the (left) regular and (right) fine mesh.

3.1. Intralaminar Damage Model

Among the fiber and matrix damage that can take place within a lamina, only the matrix damage is taken into consideration parallel to the experimental observations. An orthotropic constitutive material model that predicts damage initiation and progression is implemented in ABAQUS via user written VUMAT material subroutine [37], which is presented in Appendix section. In the material model, elastic part follows the linear orthotropic relation. Upon exceeding elastic limits, initiation and evolution of damage in an integration point are characterized by the bilinear equivalent stress (σ_{eq}) vs. equivalent displacement (δ_{eq}) relation that is represented in Figure 10.

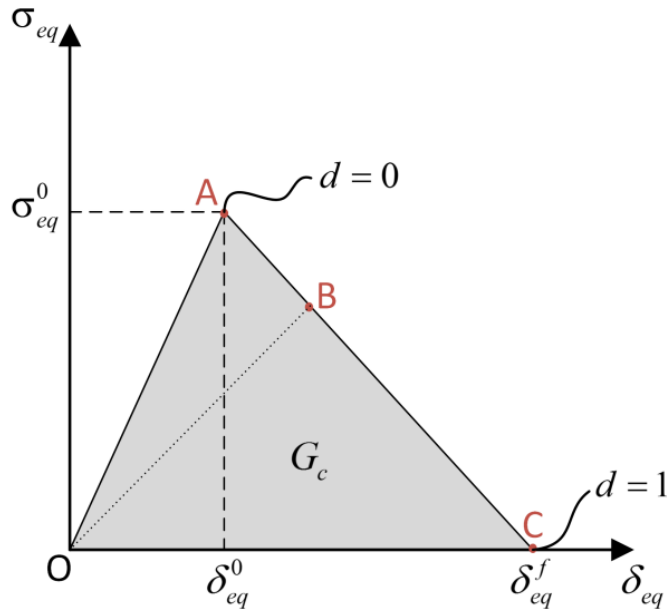


Figure 10: Constitutive response of interlaminar damage model.

3.1.1. Damage Initiation Criterion

In this study, LaRC04 failure criterion proposed by Pinho et al. [25] is employed for modeling the initiation of intralaminar ply damage. Although LaRC04 criterion allows modeling of fiber failure and matrix damage separately, fiber failure is excluded in current implementation in agreement with the experiments. The onset of material degradation for matrix failure corresponds to the point A in Figure 10, beyond which damage starts to propagate.

LaRC04 is one of the theories that was developed based on the observations of World-Wide Failure Exercise (WWFE) [38]. Different from common Hashin [39] and Puck [31] criteria, 3D formulation of LaRC04 is more suitable for the modeling of damage induced by out-of-plane loading conditions, such as transverse impact. For tensile matrix damage, LaRC04 includes a failure model derived from Dvorak and Laws's [40] fracture mechanics analysis of a crack in a lamina. Strength reduction in clustered plies due to in-situ effect [41] is also taken into account in the damage, considering the thick middle 90° layer of current model. On the other hand, compressive matrix damage criterion is based on a 3D modification of Puck and Schürmann's formulation [31]. Corresponding equations for matrix failure are presented as follows where subscripts 1 and 2 represent in-plane fiber and matrix directions, respectively, while 3 is the out-of-plane direction:

Tensile matrix failure for the case $\sigma_{22} > 0$:

$$(1 - g) \frac{\sigma_{22}}{Y_{is}^T} + g \left(\frac{\sigma_{22}}{Y_{is}^T} \right)^2 + \frac{\Lambda_{23}^o \tau_{23}^2 + x(\gamma_{12})}{x(\gamma_{12|is}^u)} = 1 \quad (1)$$

Compressive matrix failure for the case $\sigma_{22} < 0$:

$$\left(\frac{\tau^T}{S^T - \eta^T \sigma_n} \right)^2 + \left(\frac{\tau^L}{S_{is}^L - \eta^L \sigma_n} \right)^2 = 1 \quad (2)$$

In equation (1), Λ_{23}^o denotes the component of the crack tensor proposed by Laws [42] as:

$$\Lambda_{23}^o = \Lambda_{22}^o = 2 \left(\frac{1}{E_{22}} - \frac{\nu_{21}^2}{E_{11}} \right)$$

The symbol x denotes the energy released by the work done from the stress-strain relation of interior term. Accordingly, $x(\gamma_{12})$ reads the integration of the in-plane shear stress-strain curve as follows:

$$x(\gamma_{12}) = 2 \int_0^{\gamma_{12}} \tau_{12} d\gamma_{12}$$

where $\gamma_{12} = \frac{Y^T}{G_{12}}$. In this equation, integration is analytically performed with a linear stress vs. strain assumption, yielding $x(\gamma_{12}) = G_{12}\gamma_{12}^2$.

In-situ values of toughness ratio g , transverse tensile strength Y_{is}^T and in-plane ultimate strain $\gamma_{12|is}^u$ vary for thin and thick plies because of the constraining effect of adjacent plies. Experiments reveal that a defect of width 0.8 mm is named as a *slit crack* and may be inherent in a lamina as manufacturing defects [43]. In the current case, thickness of middle layer is $t = 1.8 \text{ mm} > 0.8 \text{ mm}$ and therefore the middle 90° layer is identified as a thick ply. Corresponding thick ply formulations can be given as:

$$g = 1.12^2 \frac{A_{22}^o (Y^T)^2}{x(\gamma_{12}^u)}$$

$$Y_{is}^T = 1.12\sqrt{2}Y^T$$

$$\gamma_{12|is}^u = x^{-1}(2x(\gamma_{12}^u))$$

with x^{-1} denoting derivative of the interior part and with a linear assumption $\gamma_{12|is}^u$ yielding $\gamma_{12|is}^u = \sqrt{2x(\gamma_{12})/G_{12}}$

In equation (2) representing the compressive failure criterion, the stresses σ_n , τ^T and τ^L are respectively normal, transverse and longitudinal components that act on the fracture plane, and calculated by Mohr-Coulomb criterion by considering the angle of fracture plane forming with vertical (α_0) as follows:

$$\sigma_n = \frac{\sigma_{22} + \sigma_{33}}{2} + \frac{\sigma_{22} - \sigma_{33}}{2} \cos(2\alpha) + \tau_{23} \sin(2\alpha)$$

$$\tau^T = -\frac{\sigma_{22} - \sigma_{33}}{2} \sin(2\alpha) + \tau_{23} \cos(2\alpha)$$

$$\tau^L = \tau_{12} \cos(\alpha) + \tau_{31} \sin(\alpha)$$

Although the angle α depends on loading conditions, it usually turns out to be $\alpha_0 \approx 53^\circ \pm 2^\circ$ [31], which also characterizes transverse shear strength as

$$S^T = Y^C \cos(\alpha) \left(\sin(\alpha) + \frac{\cos(\alpha)}{\tan(2\alpha)} \right)$$

For longitudinal shear stress on the other hand, in-situ value $S_{ts}^L = \sqrt{2}S^T$ is considered due to significant variation on thick laminates.

η^T and η^L represent friction coefficients at transverse and longitudinal directions. The transverse component is determined by using Mohr's circle corresponding to the case of pure compression as

$$\eta^T = -\frac{1}{\tan(2\alpha)}$$

Having obtained the transverse component, the longitudinal component can then be calculated by using the relation Puck and Schürmann [31] suggested as

$$\eta^L = \frac{\eta^T S^L}{S^T}$$

Further details of LaRC04 criterion can be found in [25].

3.1.2. Damage Evolution Criterion

Once damage is initiated in an integration point, its evolution is modeled by a linear softening response, originally proposed for cohesive elements by Camanho and Dávilla [36]. Accordingly, the growth of an initial flaw to completely damaged state follows line A-C in Figure 10. The area under the curve is characterized by the energy dissipated during failure (G_C), which is taken as energy release rate in transverse failure due to shear loading (G_{IIc}). The line B-O is followed when an unloading occurs from a partially damaged state B. Definitions of equivalent displacement (δ_{eq}) and equivalent stress (σ_{eq}) are adapted from the damage evolution formulation of ABAQUS [37] and modified for the three-dimensional elements as:

$$\delta_{eq} = L^c \sqrt{\langle \pm \epsilon_{33} \rangle^2 + \langle \pm \epsilon_{22} \rangle^2 + \epsilon_{12}^2 + \epsilon_{13}^2 + \epsilon_{23}^2} \quad (3)$$

$$\sigma_{eq} = \frac{\langle \pm \sigma_{22} \rangle \langle \pm \epsilon_{22} \rangle + \langle \pm \sigma_{33} \rangle \langle \pm \epsilon_{33} \rangle + \tau_{12} \epsilon_{12} + \tau_{13} \epsilon_{13} + \tau_{23} \epsilon_{23}}{\delta_{eq} / L^c} \quad (4)$$

The \pm term in Eqns. (3) and (4), should be taken as plus sign for tensile failure mode, i.e.: $\sigma_{22} > 0$ and minus sign for compressive failure mode, i.e.: $\sigma_{22} < 0$. L^c refers to the characteristic length defined for each element to alleviate mesh dependency and $\langle \rangle$ represents the Macaulay bracket, which is defined as $\langle a \rangle = (a + |a|)/2$.

The damage evolution is an irreversible process. In that context, the damage variable d should satisfy the irreversibility of the σ_{eq} vs. δ_{eq} curve. This behavior is implemented in the material model by the following non-linear saturation type behavior:

$$d = \frac{\delta_{eq}^f (\delta_{eq} - \delta_{eq}^0)}{\delta_{eq} (\delta_{eq}^f - \delta_{eq}^0)} \quad (5)$$

where, δ_{eq}^0 and δ_{eq}^f are the equivalent displacements at the initiation point of damage and at the completely propagated damage state, respectively. In Eqn (5), $d_m = 0$ corresponds to point A and $d = 1$ corresponds to point C in Figure 10. The saturation-type evolution of damage variable d with respect to equivalent displacement δ_{eq} is illustrated in Figure 11.

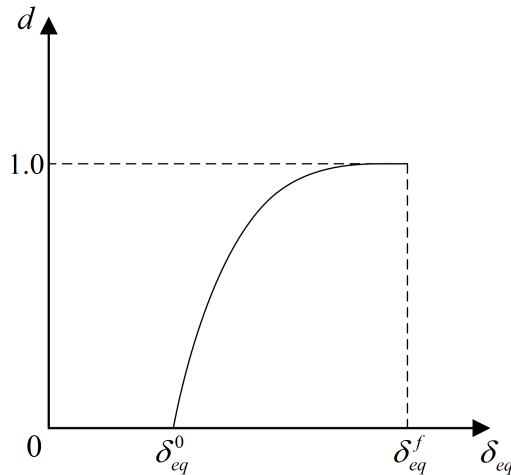


Figure 11: Saturation type evolution behavior of matrix damage variable d .

3.1.3. Stiffness Degradation Scheme

During the evolution period of the damage, stiffness is degraded according to the damaged stiffness matrix proposed by Matzenmiller et al. [44] for two-dimensional problems. For the current three-dimensional study, the damaged corresponding compliance tensor provided by English [45] is used:

$$S = \begin{bmatrix} \frac{1}{E_{11}} & -\frac{\nu_{21}}{E_{22}} & -\frac{\nu_{31}}{E_{33}} & 0 & 0 & 0 \\ -\frac{\nu_{12}}{E_{11}} & \frac{1}{E_{22}(1-d_m)} & -\frac{\nu_{32}}{E_{33}} & 0 & 0 & 0 \\ -\frac{\nu_{13}}{E_{11}} & -\frac{\nu_{23}}{E_{22}} & \frac{1}{E_{33}(1-d_m)} & 0 & 0 & 0 \\ 0 & 0 & 0 & \frac{1}{2G_{12}(1-d_s)} & 0 & 0 \\ 0 & 0 & 0 & 0 & \frac{1}{2G_{13}(1-d_s)} & 0 \\ 0 & 0 & 0 & 0 & 0 & \frac{1}{2G_{23}(1-d_s)} \end{bmatrix} \quad (6)$$

In Eqn. (6), d_m and d_s are damage variables (d) that reflect the current state of matrix damage and shear damage factor. Matrix damage is directly calculated from Eqn. (5) for either tensile d_m^t or compressive d_m^c matrix mode, according to the element being loaded in tension or compression. Shear damage factor, on the other hand, is characterized by the combination of damaged parameters as $d_s = 1 - (1 - d_m^t)(1 - d_m^c)$ [37]. Note that $d_m = d_m^t$ for $\sigma_{22} > 0$ and $d_m = d_m^c$ for $\sigma_{22} < 0$. Stresses in a damaged element are then returned by classical stress-strain relation as $\sigma = C\epsilon$, where stiffness matrix C is the inverse of compliance matrix S and ϵ being the strain tensor.

3.2. Interlaminar Damage Model

In laminated composite materials, interlaminar damage results in the development of interfacial cracks so-called *delamination*. To this end, a cohesive zone method (CZM) [36] with a triangular bilinear response as shown in Figure 12 is used for the modeling of delamination. The bilinear response of cohesive damage model is similar to intralaminar damage model shown in Figure 10. However, contrary to the intralaminar damage model, in CZM surface tractions T as a function of separations δ are defined on interfaces. In most real applications interfaces are subjected to multiaxial loading, which causes mixed mode delamination. This behavior is taken into account by

interpolation of traction-separation laws of normal and shear modes as shown in Figure 13 for modes I and II.

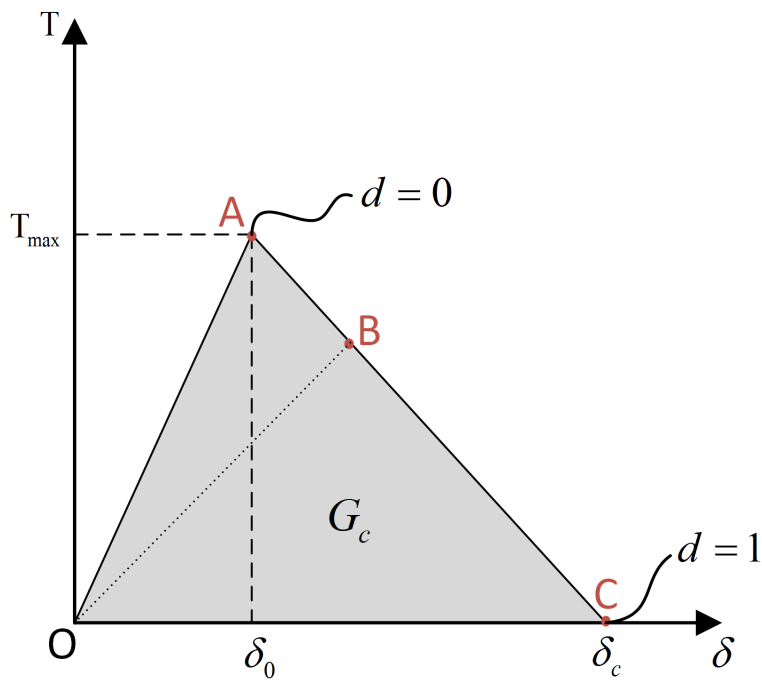


Figure 12: Bi-linear traction-separation response of the interlaminar damage model.

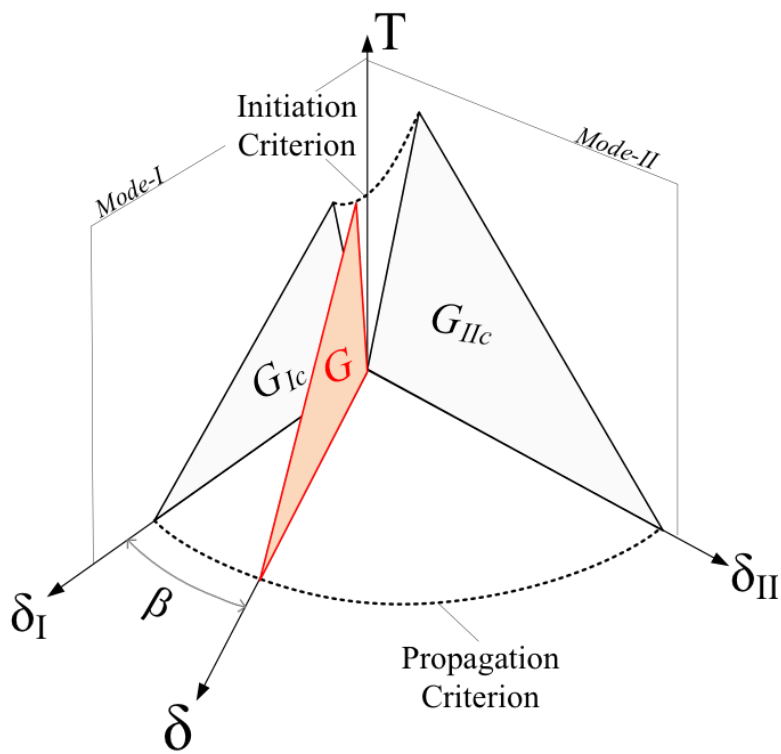


Figure 13: Mixed-mode response of interlaminar cohesive zone model (CZM).

In a pure normal or shear mode, the traction increases linearly up to the interfacial strength T_{max} at $\delta = \delta_{0,i}, i = I, II, III$, corresponding to onset of separation for a pure mode. Interfacial normal and shear strength values $T_{o,i}$ are obtained by experiments [46,47]. The initial slope of the bilinear curve is called *penalty stiffness* E_o which needs to be taken as high as possible to prevent generation of an unphysical compliance prior to onset of delamination [48].

Table 1: Interface properties of Hexcel 913C/HTS material.

Interface Strength	$T_{o,I} = 105MPa; T_{o,II} = 105MPa$
Fracture Toughness	$G_{I,c} = 260N/m; G_{II,c} = 840N/m$
B-K Criterion Constant (η)	1.45
Penalty Stiffness (E_o)	$5 \cdot 10^{14}MPa$

After the initiation of delamination, a linear softening starts where the traction goes to zero at pure mode critical displacements $\delta_{c,i}, i = I, II, III$. The area under the curve for each pure mode gives the corresponding fracture toughness G_{ic} , which are obtained by standard tests [49,50]. Knowing interfacial strength and fracture toughness for each mode the critical displacements $\delta_{c,i}$, can be easily found through the relation $\delta_{c,i} = 2G_{ic}/T_{o,i}, i = I, II, III$.

The mode-mixity is taken into account both for the onset and propagation of delamination through quadratic nominal stress criterion [37] and Benzeggagh-Kenane [51] criterion, respectively.

The quadratic nominal stress criterion is given as

$$\left(\frac{\langle T_I \rangle}{T_{o,I}}\right)^2 + \left(\frac{T_{II}}{T_{o,II}}\right)^2 + \left(\frac{T_{III}}{T_{o,III}}\right)^2 = 1 \quad (7)$$

where $T_i, i = I, II, III$ stands for tractions in each pure mode. The mixed-mode propagation criterion reads [51]

$$G_c = G_{Ic} + (G_{IIc} - G_{Ic}) \left(\frac{G_{II} + G_{III}}{G_I + G_{II} + G_{III}}\right)^\eta \quad (8)$$

where G_i , $i = I, II, III$ is the work done by the pure mode traction T_i on the corresponding separation δ_i and η is a non-dimensional curve fitting factor obtained from mixed-mode fracture toughness tests [52]. Finally, damage variable at any place on the loading curve for an element is determined using a linear damage evolution relation similar to Eqn. (5) as

$$D = \frac{\delta_c(\delta - \delta_o)}{\delta(\delta_c - \delta_o)} \quad (9)$$

where the value of mixed-mode separation at damage initiation is $\delta_o = T_o/E_o$ and its critical value is $\delta_c = 2G_c/\delta_o E_o$ with traction initiation is $T_o = \sqrt{T_{o,I}^2 + T_{o,II}^2 + T_{o,III}^2}$.

Maximum value of effective separation attained during loading history in mixed mode $\delta = \sqrt{(\delta_n)^2 + \delta_s^2 + \delta_t^2}$.

3.3. Simulations of Impact Experiments

In Figure 9a the finite element model is shown, where the steel impactor is modeled as an analytical rigid object with 0.785 kg mass and positioned just above the center of the beam. An initial downward velocity of 4.43 m/s is assigned to the impactor, simulating free fall from a 1 m height. The boundary conditions are defined in a 25 mm x 17 mm area (red areas in Figure 9a and Figure 9b) where displacements are fixed (i) in the x-direction in upper surfaces and (ii) in both x and z-directions in bottom surfaces.

The beam specimen is modeled as a three-dimensional deformable body with two mesh sizes as shown in Figure 9b. In the regular mesh, each layer is modeled with one solid element in through-the-thickness direction as commonly practiced in meso-scale composite modeling [23,24,28], resulting in a uniform mesh having elements of 0.2 mm x 0.2 mm x 0.3 mm dimensions. In the fine mesh, full-scale model is discretized by the element sizes in the length and thickness directions are halved, resulting in an element with 0.1 mm x 0.2 mm x 0.15 mm dimensions where each layer is modeled with two elements. In all of the models, delamination is simulated by cohesive elements placed at the top and the bottom 0°/90° interfaces. In the models, 8-noded linear brick elements with reduced integration and hourglass control (C3D8R from the ABAQUS library) are used for 3D elements and 8-noded three-dimensional cohesive

elements (COH3D8 from the ABAQUS library) are used at the interfaces. Large deflections during impact event that cause changes in structural stiffness are taken into account with nonlinear geometry option.

The interaction between objects is simulated by *General Contact Algorithm* of ABAQUS with kinematic constraint enforcement method for normal behavior and the Coulomb friction for tangential behavior. In addition to the interaction of the impactor and the beam, contact is also taken into account within the beam when the cohesive elements between the interfaces are removed. The friction coefficient between the steel impactor and the composite is taken as 0.3, and between the 0° and 90° layers as 0.5, according to common practice [24].

Mechanical properties of 913C/HTS material are presented in Table 2. Ply level elastic properties ($E_1, E_2, \nu_{12}, \nu_{23}, G_{12}, G_{23}$) and strength properties (Y^T, Y^C, S_{12}) are obtained from standard ASTM tests [53–55]. The remaining properties are then assumed for 3D as $E_3 = E_2, \nu_{13} = \nu_{12}$ and $G_{13} = G_{23}$. For delamination initiation, the interlaminar shear strength (τ_1^0) value is obtained from standard EN 2563 [56] test. For delamination propagation, Mode-I fracture toughness (G_{Ic}) is measured from DCB tests according to the ASTM 5528 [49] standard and Mode-II fracture toughness (G_{IIc}) is measured from the ENF test proposed by Martin et al. [57]. Mode-III fracture toughness (G_{IIIc}) is taken to be equal to the Mode-II fracture toughness (G_{IIc}).

Table 2: Mechanical properties of Hexcel 913C/HTS material.

Density	1780 kg/m^3
Elastic	$E_1 = 135 \text{ GPa}; E_2 = 9.2 \text{ GPa}; \nu_{12} = 0.30; \nu_{23} = 0.45; G_{12} = 5.5 \text{ GPa}; G_{23} = 4.5 \text{ GPa}$
Strength	$Y^T = 60 \text{ MPa}; Y^C = 205 \text{ MPa}; S_{12} = 62 \text{ MPa}; \tau_1^0 = 65 \text{ MPa}$

CHAPTER 4

EXPERIMENTAL RESULTS

Post-mortem micrograph images of six drop weight tests are presented in Figure 14. The figure shows the side view micrographs of middle 90° layers with the top and bottom 0° layers partially visible, and the arrow denoting the impact point at the center. Specimen 4 is painted with a speckle pattern for DIC analysis. A repeatable failure pattern consisting of diagonal matrix cracks at a location between the impact point and the clamped edges, followed by delaminations at the central region of the upper $0/90$ interface and the side regions of the lower $0/90$ interface is observed in all tests. In experiments, resulting damage in the front and the back faces of the laminate is characterized to be the same. Accordingly, it can be assumed that delamination propagates uniformly through the width of the specimen.

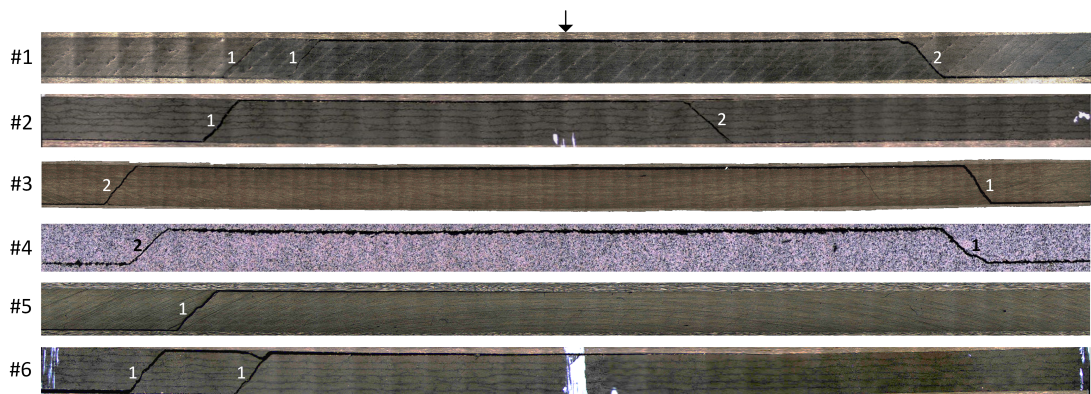


Figure 14: Micrograph images of visible central regions of damaged mid-layer of specimens.

The diagonal matrix cracks do not occur simultaneously as discerned from the high-speed camera images, and the numbers 1 and 2 on the specimen micrographs denote the sequence of matrix cracking. In general, two symmetric matrix cracks are observed as in specimens 2 – 4. However, in specimens 1 and 6, two diagonal matrix cracks are initiated simultaneously on the same side. Additionally, in specimens 5 and 6, cracks are seen to occur on one side of the specimen only. After the experiments, the specimens do not restore back to their original flat shape. Instead, a permanent

curvature remains due to the debris remaining between the failure surfaces as will be discussed later.

For the six specimens, matrix crack orientation angles, locations and initiation times are summarized in Table 3. The orientation angles of the matrix cracks vary from 46° to 56° from the horizontal with an average angle of 49° and are located at an average distance of 17 mm away from the impact point. Average initiation times of the first crack and the second crack are $268 \mu\text{s}$ and $650 \mu\text{s}$, respectfully, with an accuracy of $16.7 \mu\text{s}$. The difference between them clearly shows that cracks at different sides are formed in a sequential manner. In the following sections, impact-induced failure mechanism in $[0_5/90_3]_s$ beam laminate is investigated using high-speed camera images taken during the experiment and microscope images taken after the experiment.

Table 3: Matrix cracking sequence, angle, location and time of 6 test specimens.

Specimen #	Angle (1 st & 2 nd)	Location from Center (1 st & 2 nd)	Initiation Time (1 st & 2 nd)
1	$48^\circ / 45^\circ / 46^\circ$	15 / 12 / 17 mm	317 / 850 μs
2	$53^\circ / 45^\circ$	16 / 7 mm	283 / 600 μs
3	$56^\circ / 52^\circ$	21 / 21 mm	333 / 600 μs
4	$46^\circ / 48^\circ$	20 / 20 mm	238 / 552 μs
5	46°	18 mm	217 μs
6	$51^\circ / 48^\circ$	20 / 15 mm	217 μs
Average	$49^\circ / 48^\circ$	18.1 / 16.3 mm	268 / 650 μs

4.1. Failure Mechanism

High-speed camera images showing (a) the impactor and specimen just before impact and enlarged view of (b) intact specimen, (c) initiation of matrix cracking and (d) propagation of damage to delamination.

In Figure 15, high-speed camera images of specimen 5 recorded at 60,000 fps (interframe time of $16.7 \mu\text{s}$) of the impact event is shown. Figure 15a shows the impactor and specimen just before impact, at the instance of contact, designated by $t = 0 \mu\text{s}$. Figure 15b–d shows a close-up area denoted by the red box. Figure 15b

shows 200 μs later after impact, just before damage initiation. The next frame taken 16.7 μs later is shown in Figure 15c clearly showing the formation of a diagonal matrix crack. The final frame, shows the delaminations that have propagated to the upper and lower interfaces from the tips of the matrix crack. These pictures are a clear evidence of the failure sequence under impact loading starting with matrix cracking and leading to delamination. The failure initiation pattern is successfully reproduced in other specimens with one or two simultaneous diagonal cracks initiating randomly at left or right side, which start between 217 μs and 333 μs .

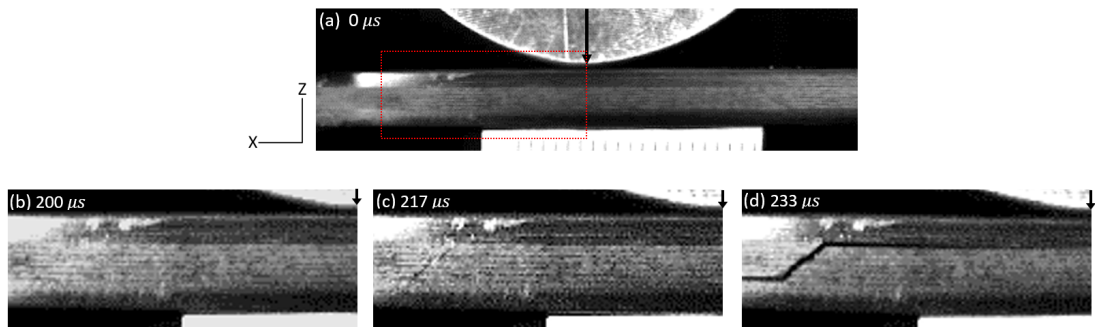


Figure 15: High-speed camera images showing (a) the impactor and specimen just before impact and enlarged view of (b) intact specimen, (c) initiation of matrix cracking and (d) propagation of damage to delamination.

The progression sequence of damage for specimen 3 is presented in Figure 16, again with images captured at 60,000 fps. The field of view consists of the total length of the specimen with the impact point shown by the white arrow at the center. Figure 16a shows the sequence of pictures just before and after the first crack initiates at the right-hand side. The first image at 317 μs shows no visible damage. Two consecutive images taken at 16.7 μs interframe time shows the matrix cracks and delaminations with the upper delamination propagating to the center and then arresting due to the compressive stresses under the impactor. The specimen dissipates some of its energy by oscillations while the impactor moves further downward until 583 μs with no further damage as seen in Figure 16b. At 600 μs left crack tip initiates and fails in a similar sequence of events as the right side, the upper delamination propagates to the center and coalesces with the existing right delamination tip. As seen in this experiment, the two cracks do not form simultaneously, but instead form sequentially with a time difference of 216 μs . In all experiments carried out, the delaminations

occur unsymmetrically as in this case with an average time delay of $350 \mu s$ between the left and the right cracks.

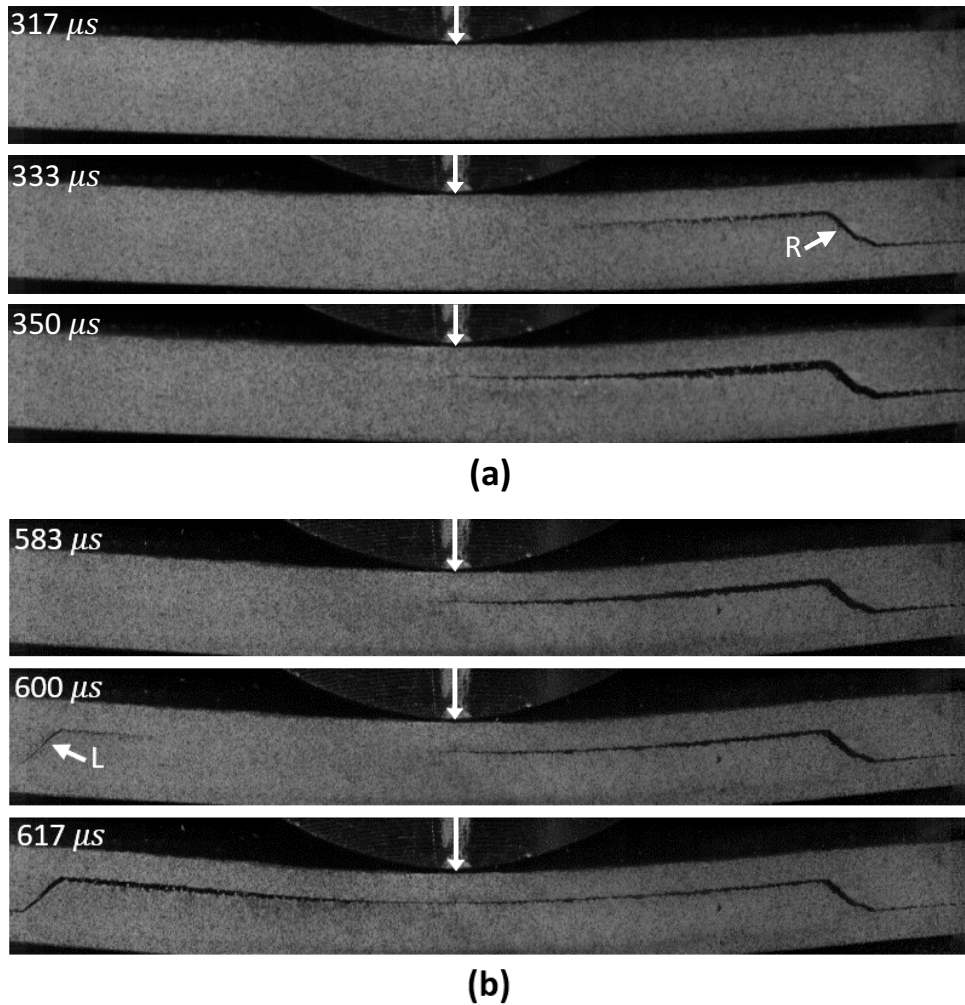


Figure 16: Typical damage initiation and propagation sequence of (a) first and (b) second crack.

4.2. Micro-matrix Cracks

DIC images using the high-speed camera are presented for specimen 4 in Figure 17. Major strain contours are shown at $266, 317, 333 \mu s$. At $266 \mu s$, there is no directionality in the major strains. However, just one frame before major crack initiates on the right hand side of the specimen, the red contours appear in a diagonal direction towards the center on both sides. This may be a sign of the local stress concentrations due to micro-cracks forming at different locations with the largest stress concentration at the potential initiation site. Finally, the crack initiates at the right side releasing the

other stress concentrations. The diagonal stress concentrations on the left side remain but are diminished.

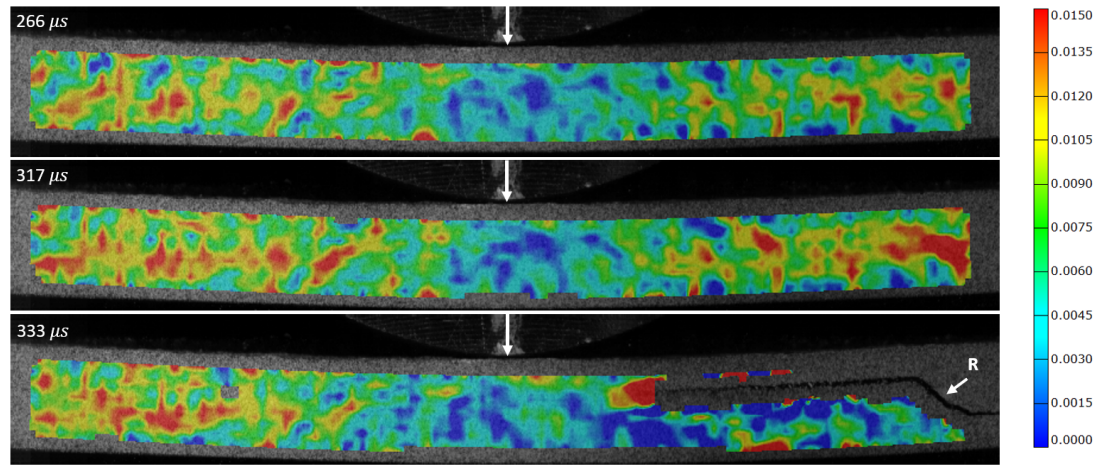


Figure 17: Major strain fields showing (top) no directionality at 266 μs , (middle) diagonal directionality just before the first crack at 317 μs and (bottom) after the first crack.

After the tests, the resulting damage is observed using the digital microscope. The top image in Figure 18 shows the side view of the specimen from the same point of view of the high-speed camera with the numbers denoting close-up microscopy images at 200x magnification. In these images, microscopic cracks can be observed with sizes ranging from 1 mm to 10 mm. These cracks are oriented diagonally, in a similar direction to the two major cracks and located along the middle layer, just below the upper interface. These cracks have similar characteristics to the ones that were schematically drawn from experiments and numerically predicted by Choi et al. [4]. However, current observations vary from the literature by being localized only at the upper layer and oriented diagonally instead of vertically.

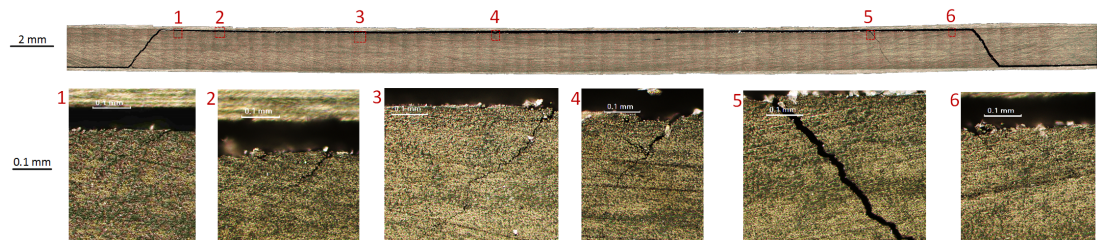


Figure 18: Micro matrix cracks observed in the neighborhood of upper interface.

Aside from the existence of the microcracks, microscopy has also revealed the reason for the permanent curvature of the damaged laminates. In specimen 5, matrix failure occurred only at the left hand side as shown in the top micrograph image of Figure 19. This allowed a detailed visualization of the crack arrest zone. A close-up of the region is shown in the middle picture, showing the permanent crack opening. A further close-up, given in the bottom left image, shows a debris particle keeping the two crack surfaces open and preventing the closure of crack surfaces. The bottom right figure presents a magnified view behind the arrested crack tip, showing partially intact regions that have not fully separated due to the compressive stresses under the impactor.

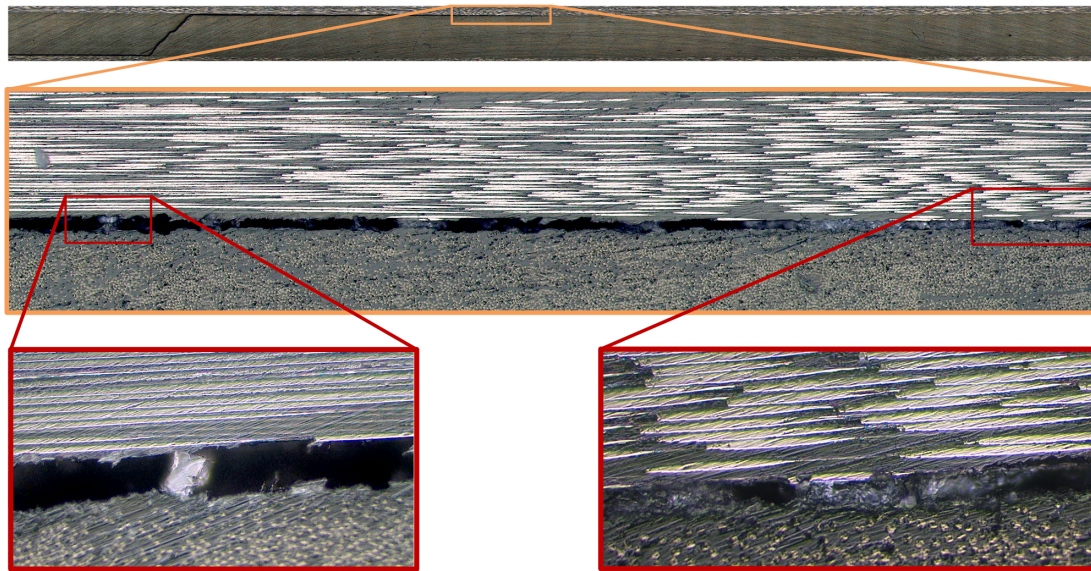


Figure 19: (Top) Upper interface of specimen 5, (Left) showing debris formation during delamination and (Right) partially intact regions near impact center.

CHAPTER 5

NUMERICAL RESULTS

Explicit finite element simulations are carried out to simulate matrix cracking and delamination failure under impact loading. Damage progression pattern and global response of the beam model consisting of load and energy histories are presented in this section. The effects of mesh refinement and symmetry modeling are also discussed in the final failure pattern, failure criterion evolution and the load vs. displacement plot.

5.1. Failure Progression Sequence

Damage initiation and formation sequence of full-scale fine mesh model is presented in Figure 20, showing the part of the model between the grips. The figure only shows the middle 90° layer and a cut-away view of the upper cohesive layer. Light gray color represents undamaged and green color represents tensile damage in bulk elements. At the interface, dark gray and red colors represent intact and partially damaged cohesive elements, respectively. When the cohesive element is fully damaged, the element is removed, revealing the light gray color of the bulk elements underneath.

- Intact interface ■
- Damaged interface ■
- Intact bulk elm. ■
- Matrix damage in bulk elm. ■

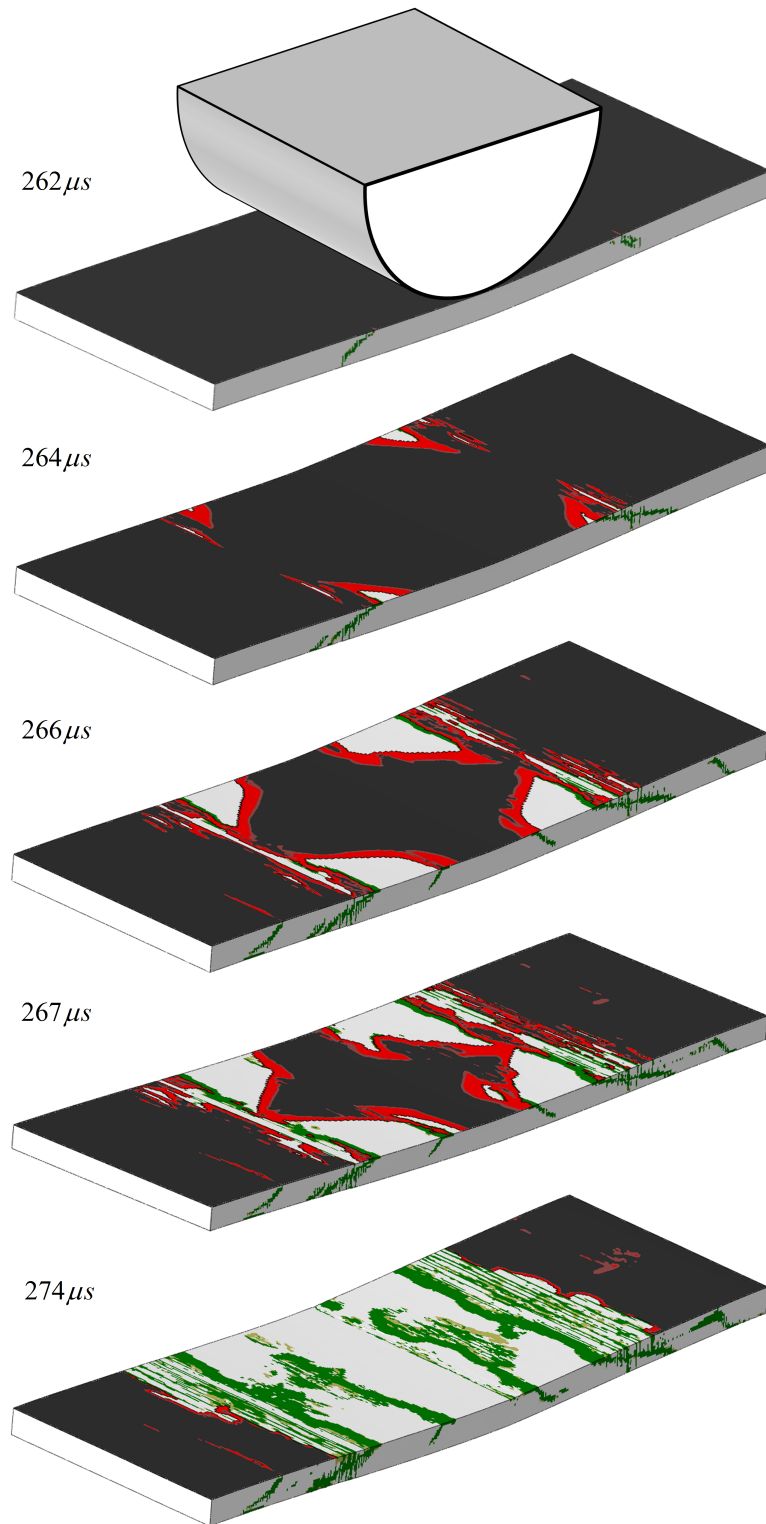


Figure 20: Three-dimensional damage initiation and propagation sequence and resulting failure pattern.

The failure sequence predicted by the simulations can be summarized as follows:

- (i) The first frame taken at $262 \mu s$ after the initial contact between impactor and the beam, shows the almost simultaneous diagonal matrix failure initiation on both the left and right sides of the impact point on the front face.
- (ii) At $264 \mu s$, delamination initiates at front and back surfaces from the tips of the matrix cracks. This pattern perfectly represents the free-edge effect, which is generally observed as stress concentrations at free-edge regions in 2D loading conditions and delamination initiation from edges [58].
- (iii) At $266 \mu s$, delamination at the four corners spread elliptically towards the center. Independently, diagonal matrix failure emerge at several elements that reside between the initial matrix cracks and the impactor. These resemble the micro matrix cracks observed in experiments (Figure 18).
- (iv) At $267 \mu s$, delaminations at outer regions start to coalesce along the width, while the secondary matrix cracks initiate secondary delaminations in front of the previous delaminations.
- (v) Damage is almost completely propagated at $274 \mu s$, where the region of the interface between the initial matrix cracks is completely delaminated, revealing the damage and undamaged bulk material underneath. In this frame, the multitude of connected matrix cracks can be observed by the green color and the intact interface by the dark grey color.

Final matrix failure and delamination pattern predicted by the simulations are given in Figure 21 for regular and fine mesh densities, in which each layer is modeled with two elements. In each simulation, three distinct matrix failure locations are predicted with the major crack in the middle connecting delaminations at upper and lower interface. Although the general pattern is similar in both models, fine mesh discretization almost perfectly predicts the micro matrix cracks that occur as 2-3 layer depth near the impactor. On the other hand, in regular mesh model, these cracks extend through the bottom interface that causes artificial delamination at the bottom interface. This seemingly insignificant effect causes an artificial increase in delamination footprint predictions, which is commonly taken as reference in residual strength calculations.

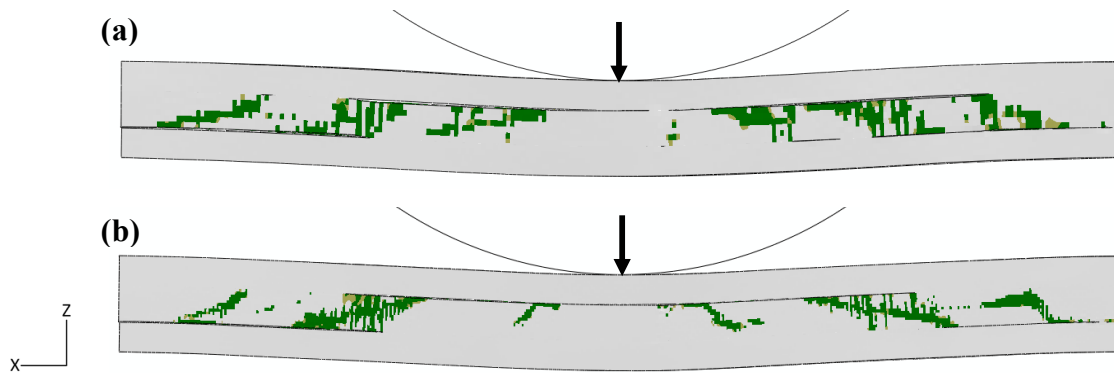


Figure 21: Matrix failure and delamination schemes when damage is completely propagated in (a) regular mesh and (b) fine mesh model.

5.2. Failure Mechanism

For better understanding the underlying mechanism behind the failure initiation process predicted by the simulations, the variation of tensile matrix failure initiation criteria is investigated along the front left half section of the unclamped region of the specimen as shown by the white line in Figure 22.

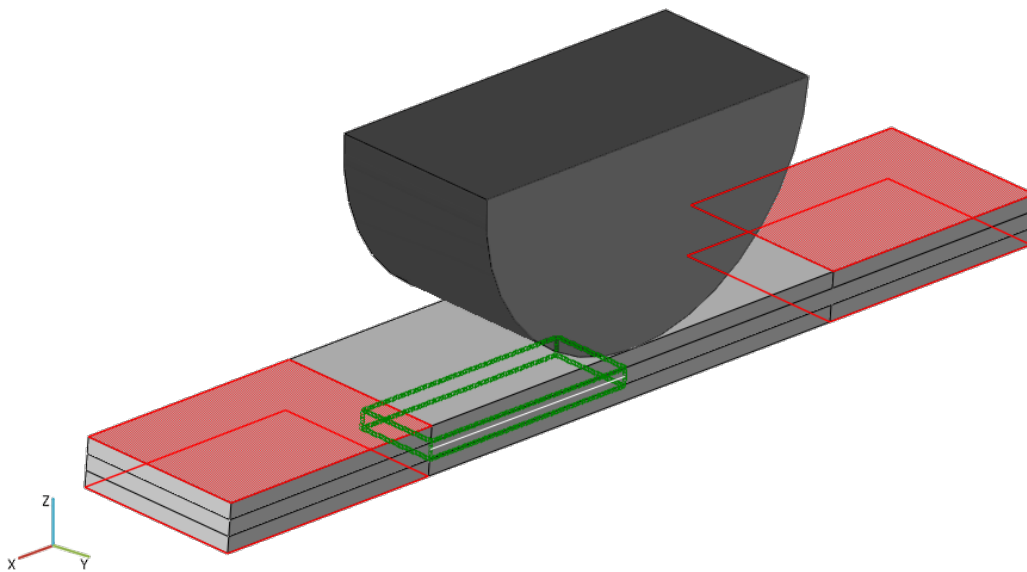


Figure 22: The path where matrix failure criterion is captured (white line).

Figure 23 shows the evolution of the failure initiation criterion at $2 \mu s$ time intervals starting $253 \mu s$ after impact. The dashed lines represent the results of the regular mesh and solid lines represent the results of the fine mesh model. The impact point is located at 0 on the right side of each plot. Since analyses have shown that the compressive

initiation criterion remains negligible until the first crack, only LaRC04 tensile failure initiation criterion given in Eqn. (1) is considered. The tensile matrix criterion value is not activated underneath the impactor and near the clamps because of the compressive stress field.

As observed in the first plot of Figure 23, the tensile failure criterion peaks to a value close to one at a time of $253 \mu s$ after impact at 18 mm away from the impact center. In the following $8 \mu s$, under wave loading, this peak diminishes and the region of peak tensile matrix criterion moves 6 mm towards the impactor, initially the peak stress falling and then rising. The damage initiates close to this point when the peak tensile failure initiation matrix criterion reaches unity at $261 \mu s$. After initiation of damage, load carrying capacity of the structure degrades in the neighborhood of the crack with a variation between the results of the two meshes. The close agreement of the results for both mesh sizes in the undamaged region is also observed in these plots, showing that there is mesh size sensitivity only after damage initiation. These results also illustrate the significance of dynamic effects under low-velocity impact in which the stress waves dynamically travel along the length of the specimen, changing the location of matrix crack initiation region drastically, and thus the total delamination area.

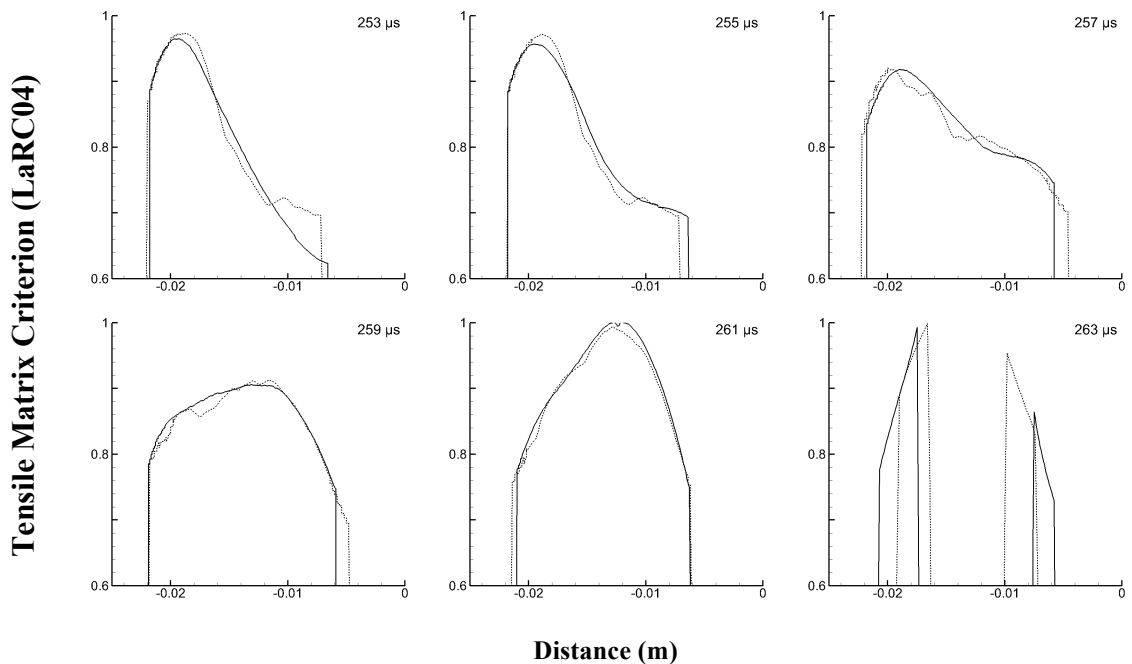


Figure 23: Evolution of tensile matrix failure criterion for regular mesh (dashed lines) and fine mesh (solid lines).

5.3. Global Response

Force-displacement response obtained from finite element simulations are shown in Figure 24. Results for regular and fine mesh models are represented by circle and triangular symbols, respectively. In the plot, the first section until point *A* corresponds to the elastic loading stage with periodic oscillations with a time period of $50 \mu s$ created by the reflection of the waves. Point *A* at $263 \mu s$ corresponds the initiation of matrix failure, with no visible effect on the curve. A steep drop on the loading curve is observed just after point *B* at $267 \mu s$, where delamination propagates throughout the width of the beam. At point *C*, load drops to almost zero, where matrix and delamination damage is propagated almost completely. After that stage, load starts to increase as the impactor moves further downward with its residual kinetic energy. In this global response, regular and fine meshed models give almost identical loading curves up to damage initiation. After damage initiation and during the post-loading stage, both curves show a similar behavior with a degree of variation in the oscillatory behavior. This general behavior is similar to the contour plots of these different models, in terms of the similarity in undamaged strain fields and the considerable difference in damage footprints.

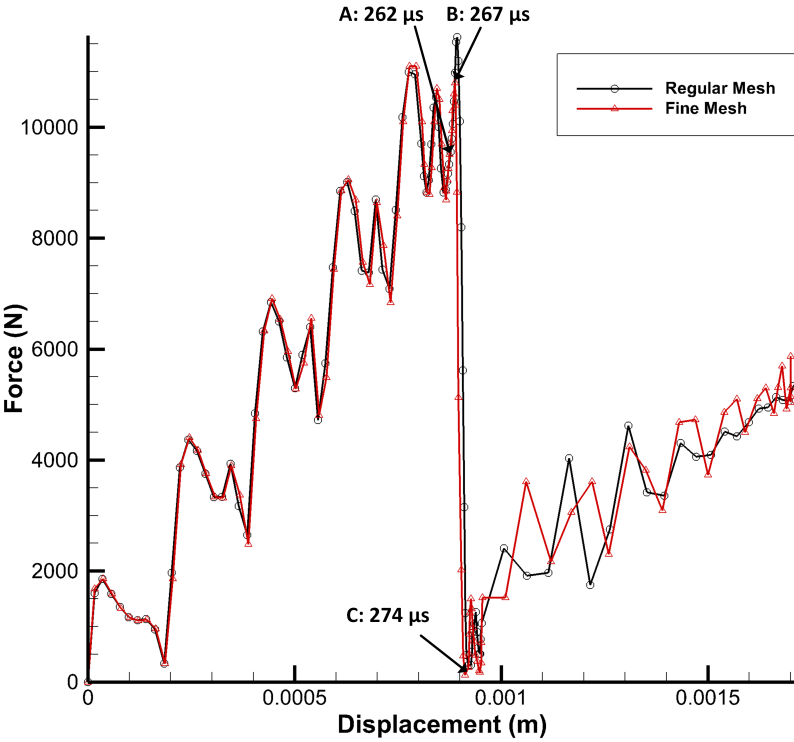


Figure 24: Load vs. Displacement responses of regular and fine mesh models.

During the impact event, initial energy of the impactor is transformed to various components as given in Figure 25 for regular and fine mesh. Until the initiation of failure, kinetic energy is transferred to the beam in the form of strain energy. With the initiation of failure at $263 \mu s$, a fraction of the strain energy converts to damage dissipation energies. Initially, failed bulk elements at outer surfaces create matrix failure dissipation, followed by a rapid increase in delamination dissipation as it is simultaneously triggered. Although delamination completely propagates at about $275 \mu s$, matrix damage in 90° layer continues to propagate towards nearby elements until about $325 \mu s$. A small amount of energy is dissipated due to friction between delaminated surfaces. Total energy throughout simulation remains almost constant, showing that simulation is not significantly affected by artificial disturbances.

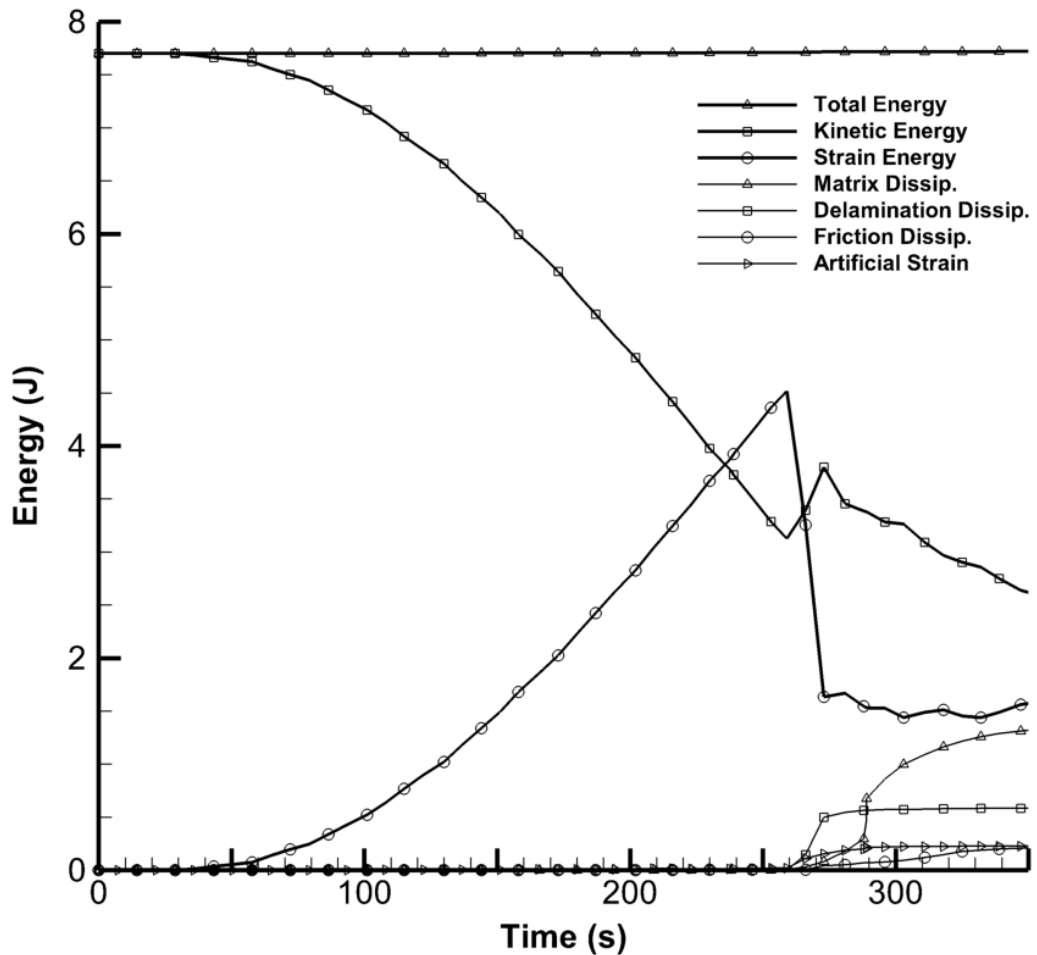


Figure 25: Evolution of energy parameters in the system with time, starting from the impact instance.

5.4. Full-Scale Model vs. Symmetric-Half Model

Symmetric modeling is a commonly employed technique in practical and research applications to increase computational efficiency by reducing the total number of elements in a computational model. In current study, the effect of symmetric modeling on the damage evolution process is investigated by creating a half model discretized with regular mesh density. In this symmetric-half model described in Figure 26, symmetry boundary conditions are defined at the half-span of the beam.

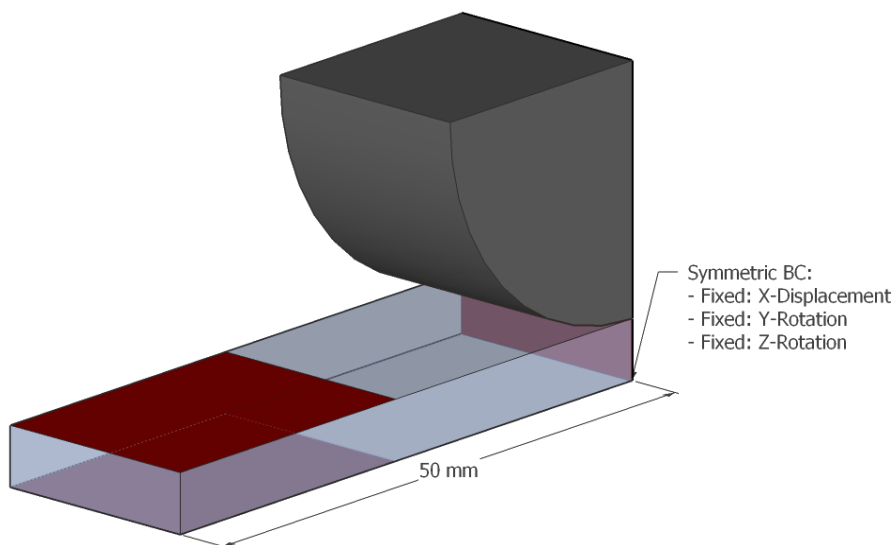


Figure 26: Symmetric-half model used in the simulations.

The results of the symmetric-half model are compared with the full-scale regular mesh model as they both have equal mesh density. In Figure 27, damage schemes of these models are presented when damage is completely propagated in a similar manner to the regular vs. fine mesh comparison given in Figure 21. Although delamination footprint results are almost same in both of the results, symmetric-half model predicted a more localized matrix failure connecting the upper and lower delaminations. The localization of matrix failure resulted in no damage near the impactor with very few failed elements near the boundary. Accordingly, symmetric-half model yielded a less accurate final damage scheme with the absence of micro-matrix cracks near the impactor.

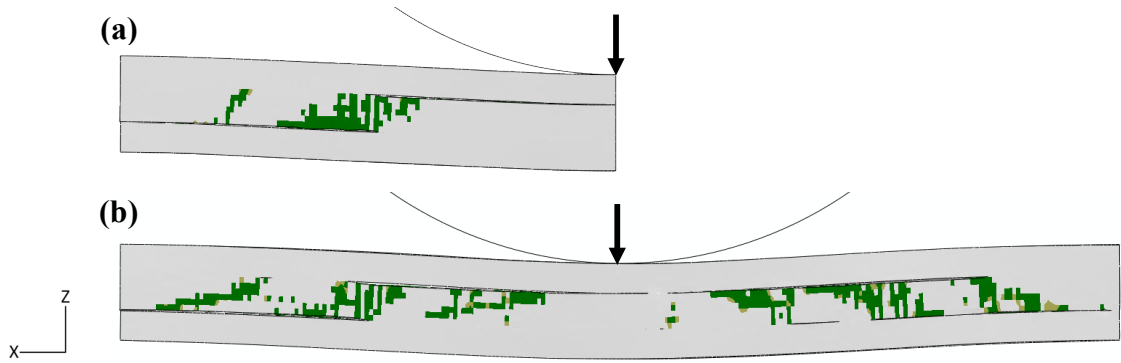


Figure 27: Final matrix failure and delamination schemes in regular meshed (a) symmetric-half and (b) full-scale models.

Following the final damage scheme, damage initiation process is also investigated in the symmetric-half model and the results are compared with the aforementioned full-scale model in Figure 28. Similar to the previous observations, the undamaged curves of both models are again very similar as seen at $253 \mu s$. Nevertheless, An almost negligible excess stress in the symmetric-half model caused the symmetric-half model to meet the LaRC04 criterion and fail earlier at $255 \mu s$, while the full-scale model remained intact at that time. As opposed to the previous full-scale models, the initial failure in the symmetric-half model did not completely propagate, and the beam continued to carry further load. The second failure that occurred after $259 \mu s$ caused the beam to fail completely from a similar location of the full-scale model.

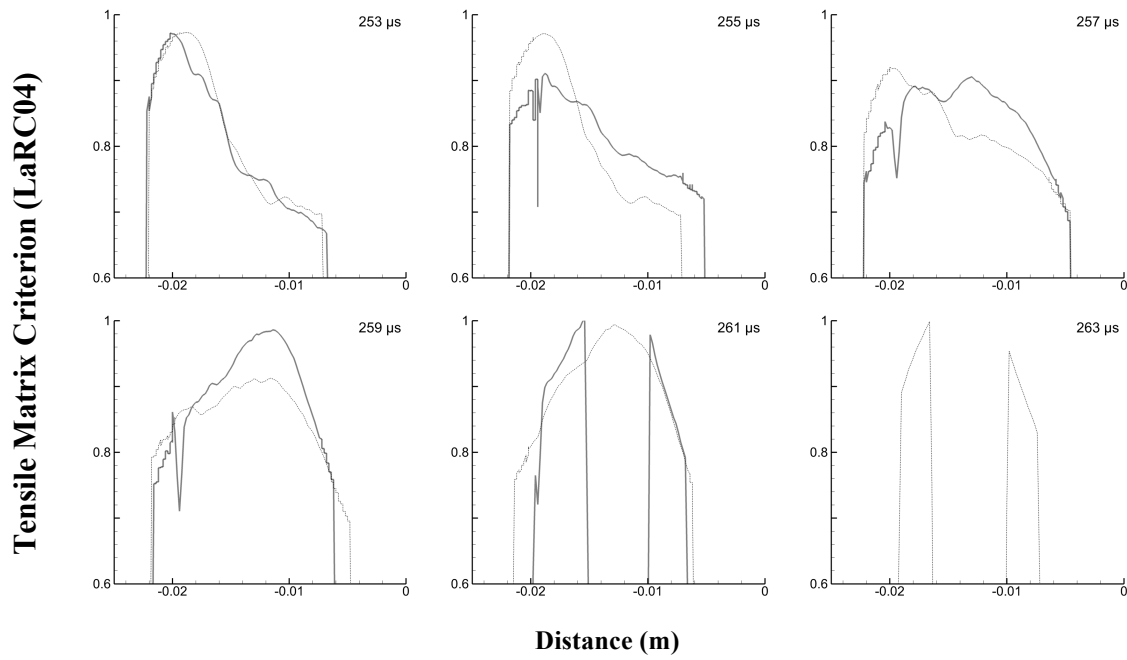


Figure 28: Evolution of tensile matrix failure criterion in the regular meshed symmetric-half (bold lines) and full-scale (light lines) models.

Finally, general response of the models are compared in the load vs. displacement plot given in Figure 29. As expected by the equal mesh densities of the models and the symmetry definition, the curves are on top of each other at elastic undamaged region. After the initial failure occurring near $11600N$, a considerable variation is observed between the responses, with a similar oscillatory behavior. This variation is sourced from the varying damage initiation times and locations as previously demonstrated in Figure 28.

Comparison of symmetric-half and full-scale models yielded a similar conclusion obtained from the comparison of regular and fine mesh models. In both of the comparisons, a slight variation between the results, which is inherent in different finite element discretizations, caused a major difference in the resulting matrix failure patterns and the total delamination area. Therefore, it can be argued that symmetry definitions might lead to inaccuracies in damage predictions, similar to the situation with the mesh refinement.

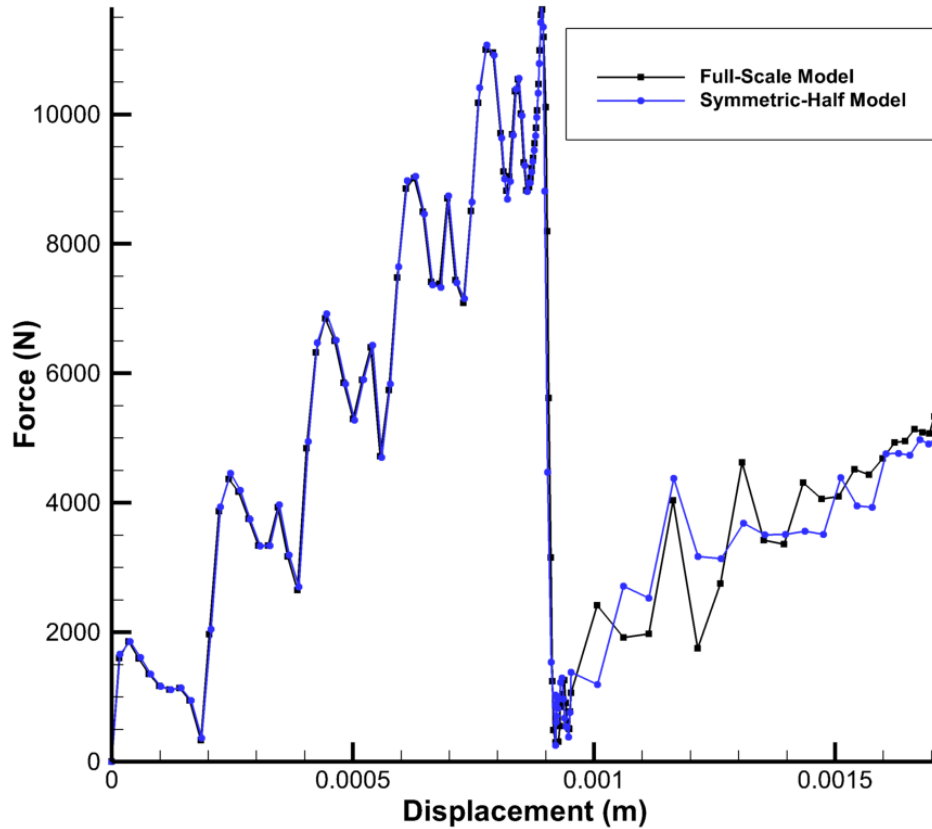


Figure 29: Load vs. Displacement responses of symmetric-half and full-scale models.

5.5. Effect of Mesh Symmetry

Contrary to the sequential damage scheme observed in experiments, numerical analyses simulated an almost symmetrical damage formation process. One of the most probable reasons of this discrepancy is assumed to be the possible experimental inaccuracies, such as an uncentered impact, uneven clamps or microscopic imperfections in the material, as opposed to the perfectly symmetric computational models.

In this section, simulation of a similar delay between left hand and right hand cracks is aimed by modifying the regular mesh used in the simulations. Figure 30 presents four different mesh patterns and impactor placement conditions that are compared. In that figure, (a) represents the regular mesh employed in the aforementioned sections. (b) is also a symmetric mesh discretization, however the impactor is in line with the center of the element instead of the node. In model (c), the nodes just below the impactor are moved 0.05 mm towards $+x$ direction, creating an unsymmetric mesh. In (d), the beam is modeled with two distinct mesh sizes. Left hand side is meshed

with regular sized elements and right hand side with fine elements, where characteristic size in length and thickness directions are halved as in previous fine mesh models. Finally in (e), the beam is partitioned into 3 equal length sections with planes rotated 60° from the horizontal. This modification resulted in an asymmetric but a regular meshed model with diagonally oriented elements. In all of the models, the impactor location is not modified, resulting a completely symmetric impact at the center of the beams.

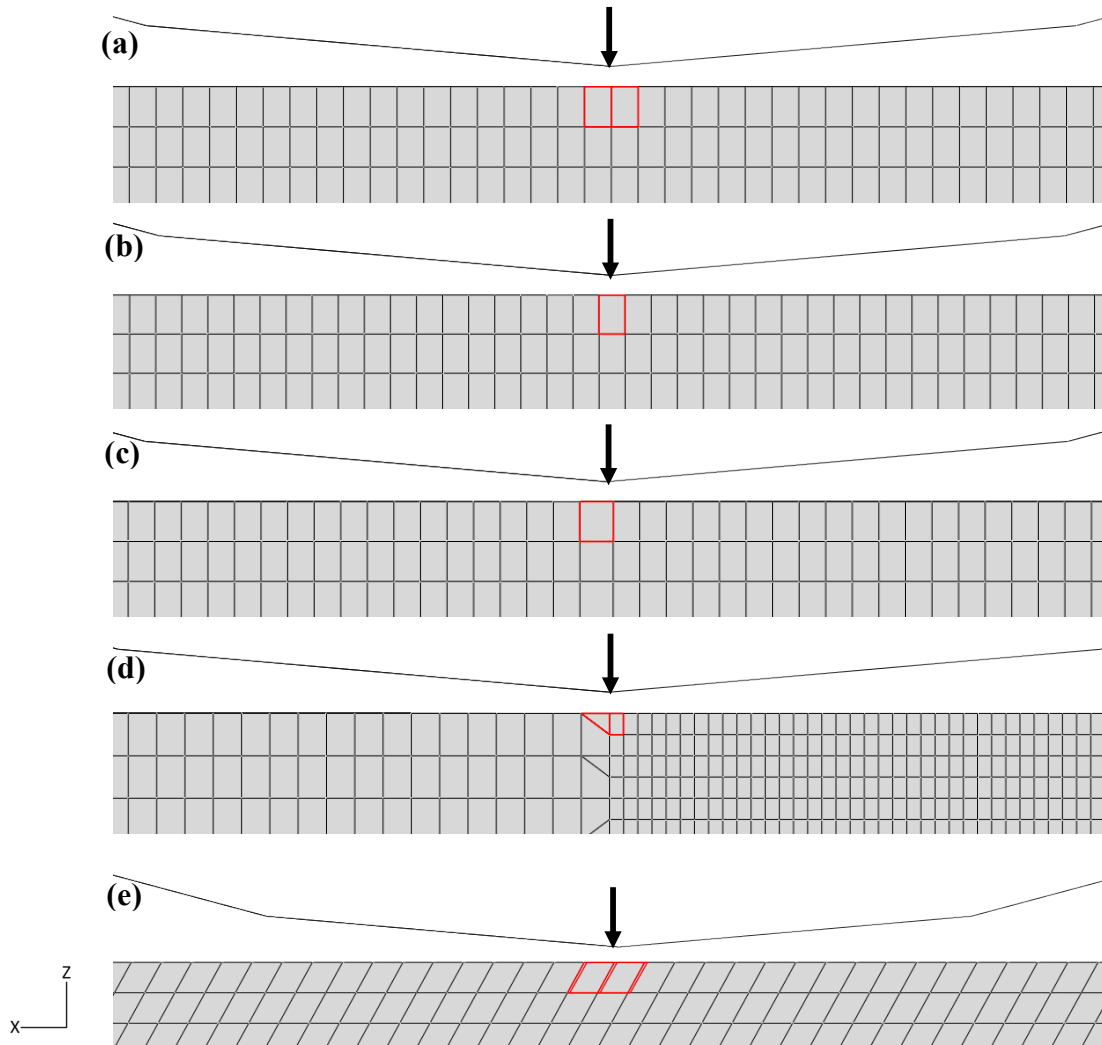


Figure 30: Five different mesh patterns of the beam and impactor positioning above the beam. (a) regular mesh with impactor placed above a node, (b) regular mesh with the impactor placed above an element, (c) unsymmetric mesh with larger elements just under the impactor, (d) unsymmetric mesh with two distinct mesh size and (e) unsymmetric mesh with diagonal elements.

Failure patterns of each model at the damage initiation instance are presented in Figure 31. It is noticed that the time resolution of the simulation is not adequate to capture any sequential behavior in the regular mesh models given in (a) and (b), in which the impact point is translated from the node to the centre of the element. Nevertheless, a sequential behavior is observed in the unsymmetric mesh models (c), (d) and (e) in the given time resolution. In model (c), failure is initiated as a diagonal crack at the left hand side, followed by the right hand side crack originating $1 \mu s$ later. Similarly in (d), failure is initiated at the right side as two diagonal lines at an earlier time than of the previous models. About $3 \mu s$ later, left and right micro cracks followed the initial ones. Finally in (e), failure is originated from the left hand side in a much steeper angle, in the element stacking direction. After $1 \mu s$, this left crack is followed by right ones in a lower angle. The effect of mesh variation on the damage process is clearly observed in the simulations. However, current mesh modifications remained unable to simulate a sequential behavior with $300 \mu s$ delay as observed in the experiments.

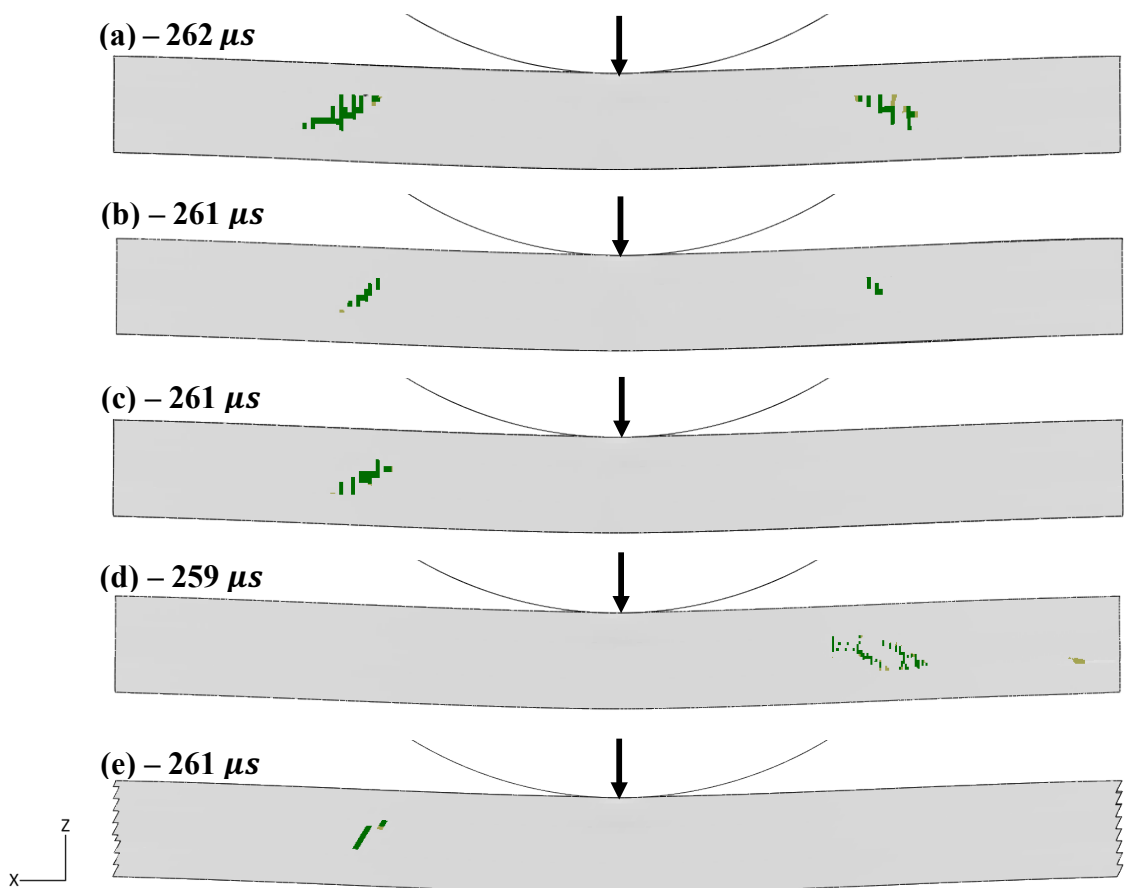


Figure 31: Matrix failure in the models given in Figure 30 at the failure initiation instances.

Damage schemes of these simulations at the time when damage has almost completely propagated are given in Figure 32. In this figure set, (a) replicates the damage scheme given in Figure 21a. In terms of damage propagation time and general failure scheme, all of the mesh modifications resulted in a similar trend to the original model. However, a noteworthy asymmetry in the failed elements, with a variation in the amount and location of the micro-cracks is observed. In model (b), micro-crack prediction on the left hand side is not propagated up to the bottom, while on right hand side, the micro-crack is extended almost towards the center of the specimen. Final failure scheme of model (c), in which the impact point is also corresponds to an element, resulted to be similar. On the other hand in model (d), where mesh is significantly irregular in the transition region, a similar damage scheme is obtained with a greater detail. However, that simulation is terminated by ABAQUS at $285 \mu s$ due to excessive distortion in the elements. In model (e), which is meshed by diagonal elements, crack is followed a path in the element direction, and a significant variation between the left and right hand major crack angles is observed.

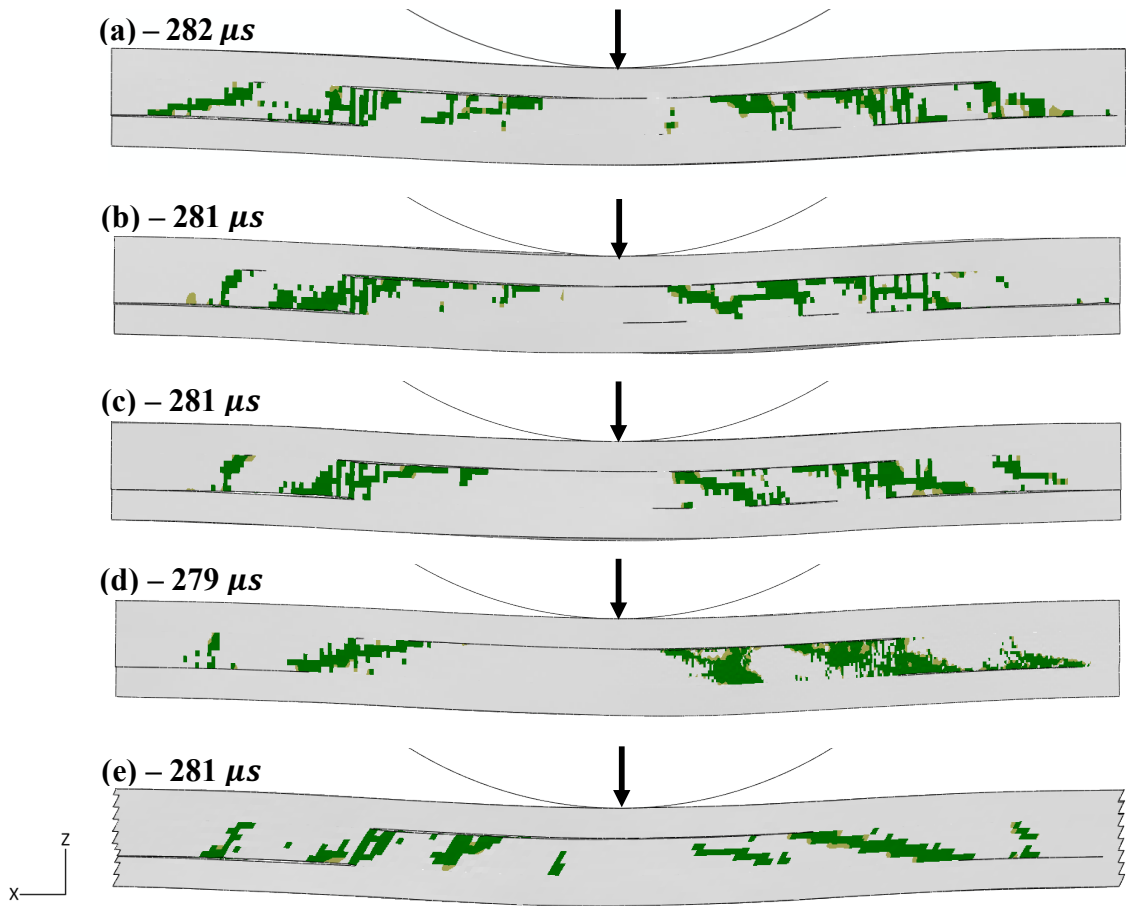


Figure 32: Matrix failure in the models given in Figure 30, once damage is almost completely propagated, 20 μs later than corresponding damage initiation.

CHAPTER 6

DISCUSSION

In this section, comparison of the results of the experiments and the simulations are presented.

Contours of transverse engineering shear strain (γ_{yz}) for DIC analysis of specimen 4 (Figure 33a) at $317 \mu s$ is compared with finite element analysis predictions (Figure 33b) at $259 \mu s$, in which those times correspond to the times just before crack initiation. The field of view for the contour plots corresponds to the rectangular region marked by the red dashed lines between the clamps shown in Figure 6. The shear strain γ_{yz} is chosen for comparison because of the dominance of τ_{yz} to the matrix crack initiation criterion shown in Eqn. (1). For both experiments and simulations, the contours show zero shear strain in a columnar region below the impact location shown by the green color. On both sides of this region, the shear strain increases sharply reaching an almost steady value of about ± 0.020 in a short distance towards the edges. A very good agreement, both qualitatively and quantitatively, between experimental DIC and FEM results is observed. The simulated shear strain contours at $259 \mu s$, which is the time after matrix crack initiation, are shown in Figure 33c. The cracks on the left and right side initiate symmetrically at 10 mm from the center at the point of maximum shear stress, almost simultaneously in the simulations contrary to the experimental observations.

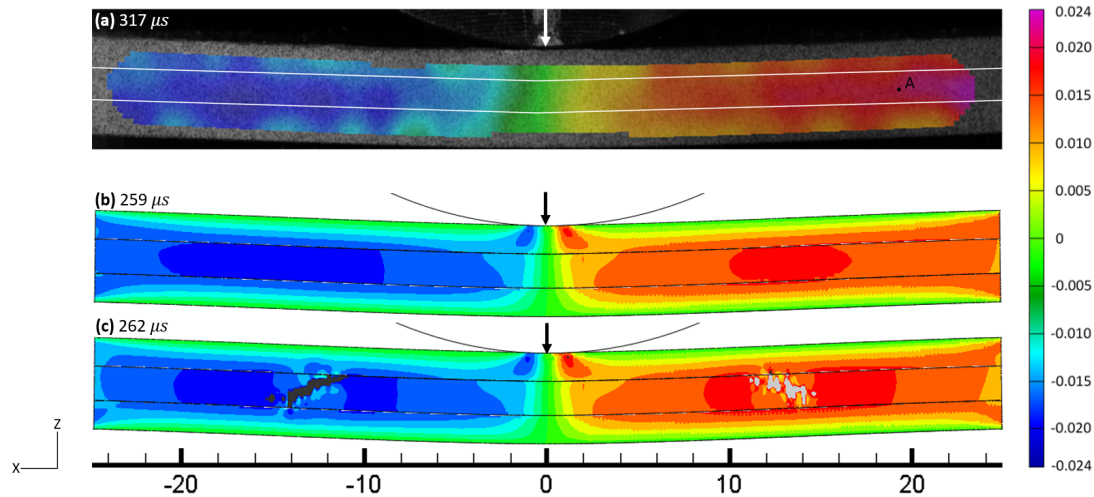


Figure 33: Transverse engineering shear strain (γ_{yz}) contours of (a) DIC analysis, FEM simulations (b) just before crack initiation and (c) just after crack initiation.

The transverse shear strain distribution along the centerline of the 90° ply is shown in Figure 34 plotted together for experiments and simulations. The thick line represents the results generated from post-processing of experimental DIC results at $317 \mu s$, corresponding to the time just before crack initiation. The thin line represents the results from FEM analysis at $257 \mu s$, also just before crack initiation. Both curves pass near the zero point at the center exhibiting a flat region of constant strain for a distance of 2 mm . The curves initially rise steeply from the center and levels towards the edges as mentioned in the previous figure of the contour plots. Small fluctuations in the shear strain in the experiments is attributed to the noise inherent in the DIC analysis. Both curves reach similar levels of maximum strain around ± 0.02 . The simulations seem to capture the basic form of the strain variation seen in the experiments.

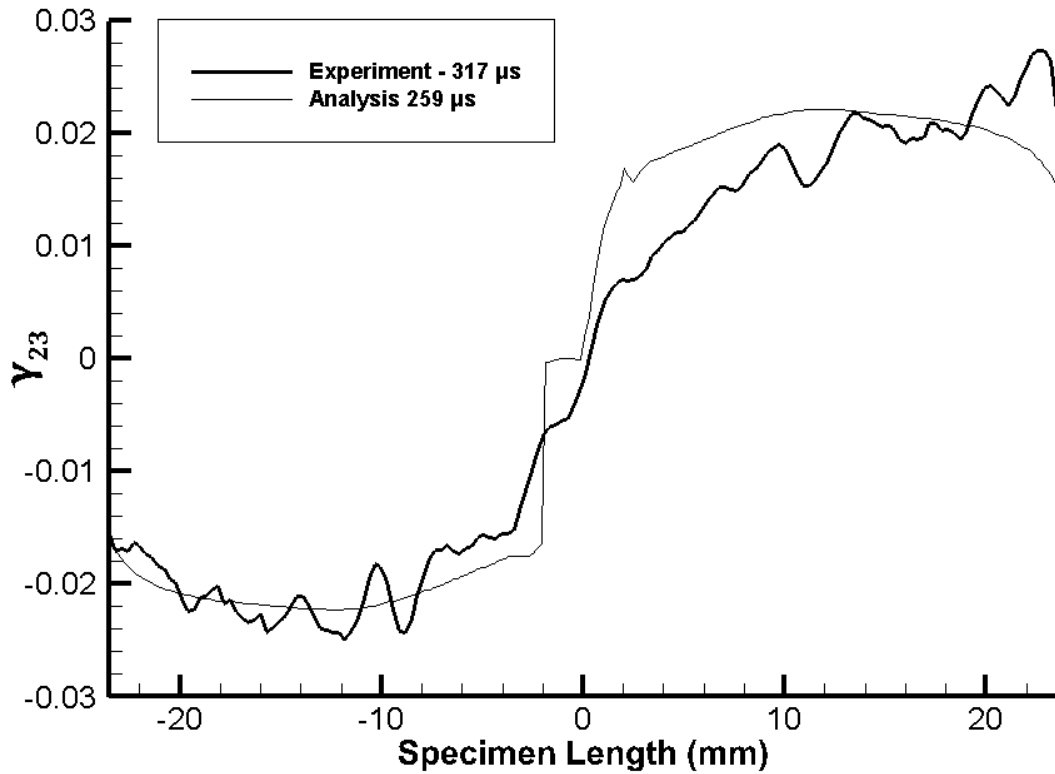
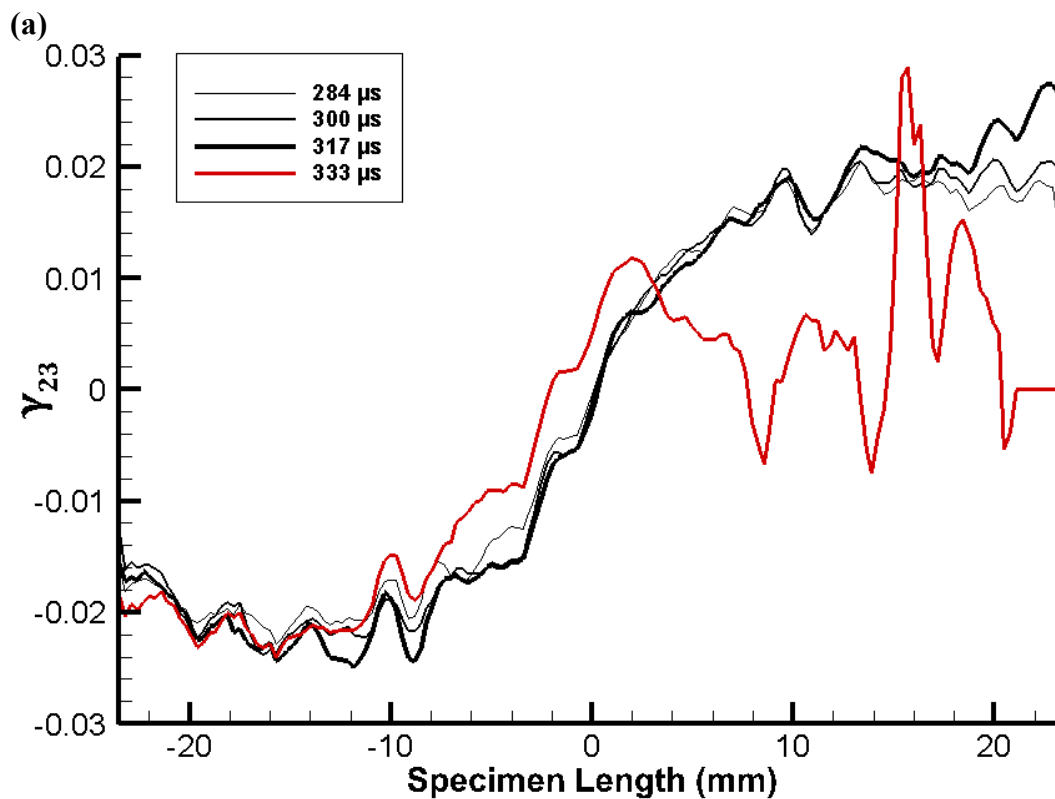


Figure 34: Transverse engineering shear strain evolution (γ_{23}) along the centerline in experiments and simulations.

Figure 35 shows a time sequence of the shear strain distribution obtained from experiments (Figure 35a) and FEM simulations (Figure 35b). Both plots show the evolution of the shear strain at different times up to crack initiation with $16.7 \mu s$ interval, corresponding to the 60,000 fps camera speed of the experiments. The black lines correspond to the strains at times before the first crack initiation and red line corresponds to the strains at the first frame after crack initiation. In Figure 35a, the strain levels gradually increase with time followed by a sudden increase at the right end at $317 \mu s$ (thick black line). At $333 \mu s$, following the nucleation of crack at the rightmost region, a sharp drop in the strains are observed with large fluctuations on the right half of the specimen depicted by the red line. Contrary to the right half, on the left half, after the crack nucleation on the right hand side some relaxation is observed in the strain state without changing the shape of the curve. This relaxation behavior allows the specimen to be further loaded for about $400 \mu s$ before failure of the left side occurs, as noted in the experimental section.

The results of simulations are depicted in Figure 35b, where the strains are observed to increase gradually with time, similar to the experiments. Failure then initiates from the point of maximum strain at 12 mm away from the center. At 274 μs , after the failure has almost completely propagated, there is a relaxation of strain throughout the 90° layer, with large fluctuations near a value of zero represented by the red line. Although these numerical predictions of the location and time of failure initiation are not in perfect agreement quantitatively with experiments, the general trends are in excellent agreement with each other. Furthermore, the numerical simulations predict simultaneous failure initiations at each side of the impact location within the available time resolution of the simulation output. This discrepancy between the simulations and the experiments can be attributed to the perfect symmetry of the finite element model versus the inherent material heterogeneity and unsymmetry in the experimental loading conditions.



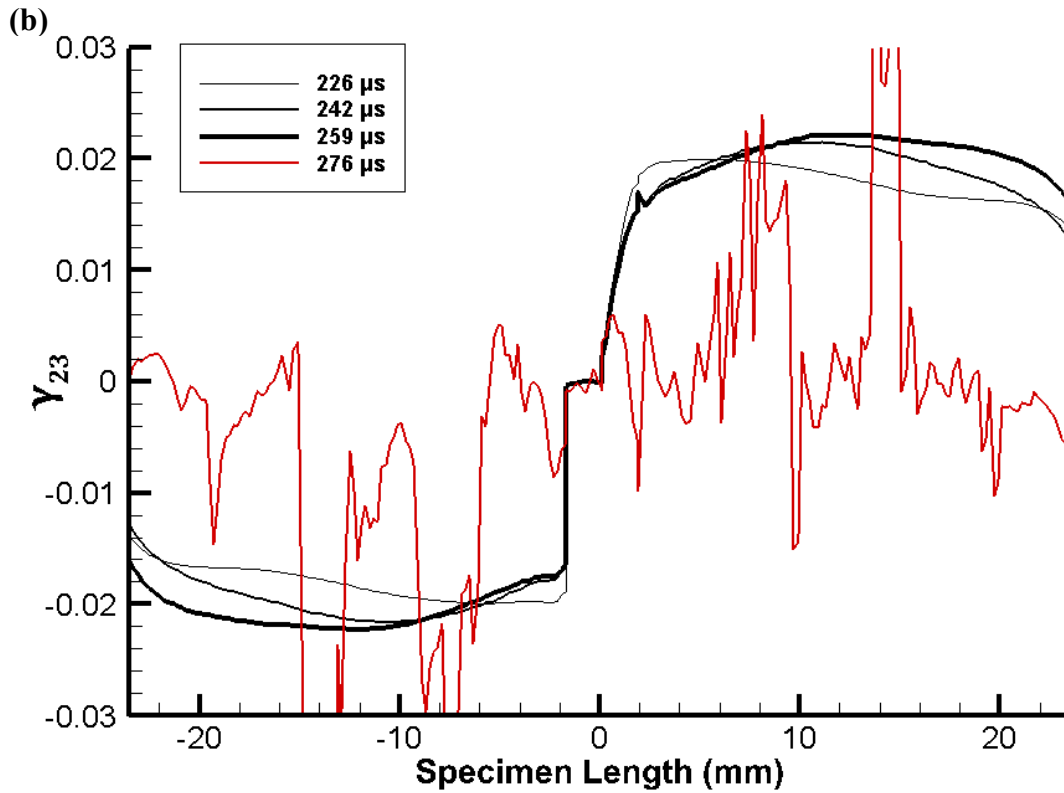


Figure 35: Evolution of transverse shear strain (γ_{23}) along the centerline with 16 μs interframe time in (a) experiments and (b) analysis.

In Figure 36, the evolution history of transverse engineering shear strain (γ_{yz}) of point A, depicted in Figure 33, is presented. In both the simulations and experiments, the strain increases in an undulating manner with an approximate time period of 50 μs , corresponding to the time period of the flexural waves in the composite. Both curves reach an approximate value of 0.024 before failure initiates and the strain drops suddenly. Again the numerical and experimental curves can be considered to agree very well with each other except in time.

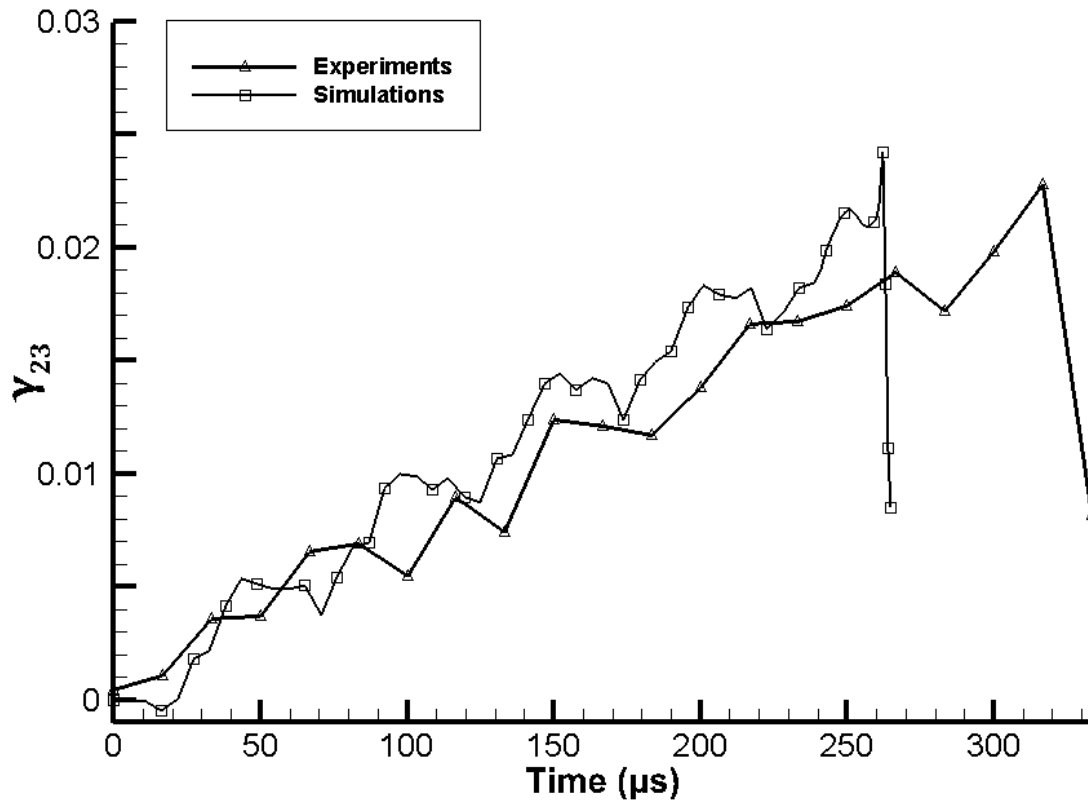


Figure 36: Evolution of shear strain obtained from DIC and FEM at the point A shown in Figure 33.

Damage initiation and progression are further elucidated in Figure 37, where a 17 mm damage process region of simulations and experiments is presented. The pictures obtained from simulations are presented on the left side of Figure 37. At 262 μs , a clear picture of the initial formation of diagonal matrix damage can be seen followed by its progression to delamination at 267 μs . The experimental high speed camera pictures for specimen 2 at two different times are shown on the right side of Figure 37. At time 217 μs , a diagonal line forms near the left end of the picture giving a conclusive evidence for matrix crack initiation under impact loading. At time 233 μs , which is the next frame time, clear evidence of delamination from the tips of the matrix crack at the top and bottom 0/90 interfaces is presented.

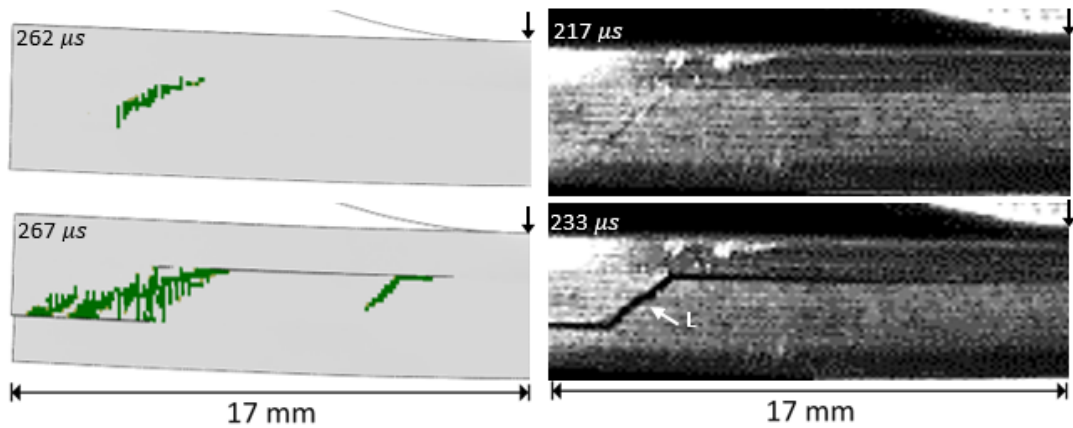


Figure 37: Matrix failure initiation and delamination propagation obtained from simulations (left) and experiments (right).

Delamination footprint of experiments and FE simulations are superposed in Figure 38, with the top and bottom 0/90 interfaces shown on the top and bottom pictures, respectively. Experimental delamination area is based on the assumption of interfacial failure being uniform along the width, where the delaminated area is determined by averaging the delamination regions of all specimens. The red dashed line envelops the experimental delamination region. In the simulation results, intact cohesive elements are represented by dark areas, while the bulk material underneath the failed cohesive elements is shown in light gray. In other words, light gray color corresponds to the delamination area. At the upper interface, a rectangular symmetric delamination region is observed in both the experiments and simulations. At the bottom interface, both the experiments and the simulations show two symmetric regions of delamination on each side with a larger delamination area predicted by the simulations, extending underneath the clamps. Also, fully and partially damaged cohesive elements around the center of the bottom interface are predicted only by the simulations. Overall, these results suggest a good agreement between the simulations and the experiments in terms of total delamination area occurring at the lower and upper 0/90 interfaces.

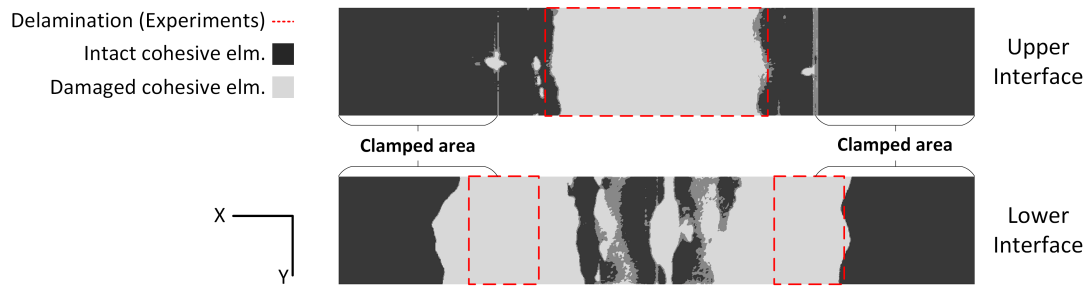


Figure 38: Delamination footprint of experimental average and prediction of FE analysis.

6.1. Effect of Matrix Failure Properties on Failure Initiation, Angle and Time

The experiments presented in Table 3 show a variation in matrix damage location, angle and time that is not insignificant even though the experiments are conducted on the same batch of material. In Figure 39a, the first cracks obtained from the experiments are superimposed schematically on the left side of the specimen showing the extent of variation in the location and angle. To investigate this variation, impact simulations are conducted on models with 2% reduced and increased strength properties of 3D solid elements, as it is expected that brittle epoxy material can be inherent such variation. The results of the simulations are shown in Figure 39b where the matrix failure initiation schemes on the left side are shown. The matrix failure patterns for the original, the strong and the weak material properties are represented by green, red and blue colors, respectively. A notable variation in failure locations, as expected due to the dynamic translation of stress fields as in Figure 23 is observed in the analyses. Strong material results in a crack with about 55° angle, initiating $4 \mu\text{s}$ later than the original, while the weak model yields an almost 30° angle, initiating $7 \mu\text{s}$ prior to the original one.

In simulations, a significant departure from the original result is reproduced by creating a minimal variation in the material properties. The deviation range of crack angle and location is successfully simulated, while the major time discrepancy is not completely replicated. As a final note, the variation in matrix crack location predictions leads to a variation in the total delamination area, which strongly affects the residual strength of the structure. This behavior is a clear demonstration of the difficulty in reproducibility and accurate predictability of dynamic failure of composites.

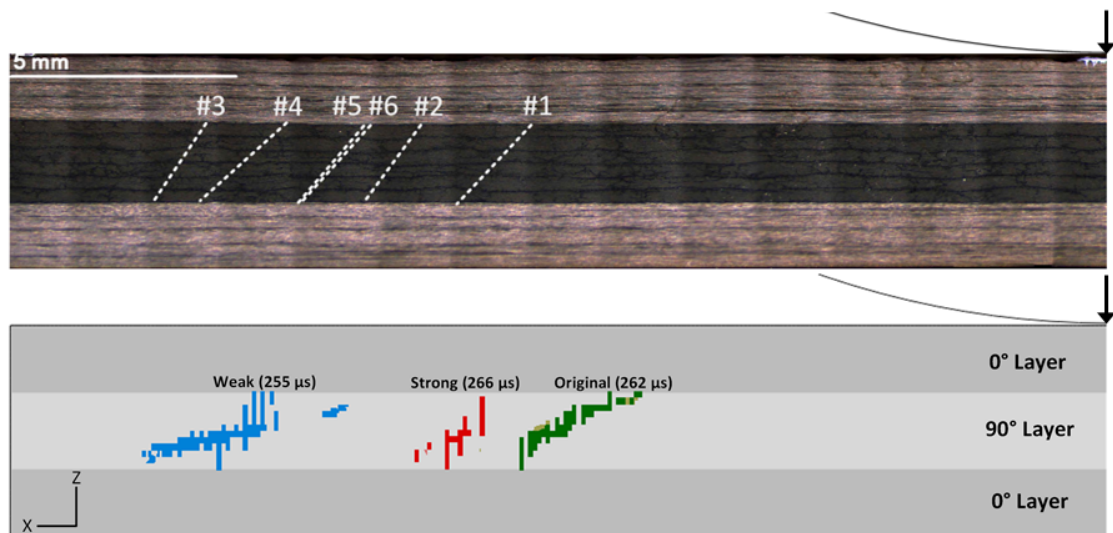


Figure 39: Damage initiation locations; (top) observed in six specimens and (bottom) obtained from simulations with 2% weaker and 2% stronger material properties, with initiation times. Results are normalized at the left side.

CHAPTER 7

CONCLUSIONS

In this article, the dynamic failure process of composite laminates under low-velocity impact is studied using a combined experimental and numerical approach. Impact experiments are carried out on a thick $[0_5/90_3]_s$ CFRP beam laminate and damage process is studied by a high-speed camera imaging, DIC analysis and microscopy. In explicit FE simulations intraply matrix cracking is considered in a 3D Continuum Damage Mechanics (CDM) framework and delamination is considered through cohesive elements. The main conclusions are summarized as follows:

- 1) First experimental evidence of the failure sequence in 2D loaded $[0/90]_s$ laminates is presented consisting of diagonal matrix cracks followed by delamination. The right and left matrix cracks are shown to occur sequentially with an about $350 \mu s$ delay on the left and right sides of the impact point.
- 2) In the experiments, several micro-cracks parallel to the major matrix crack direction are observed at the top of the middle layer. The orientation of these micro-cracks is in agreement with the FE simulations, as well as with the computational results in [22]. The directionality in DIC results just before the initiation of major matrix crack giving evidence that micro-cracks form before the initiation of delamination.
- 3) Results of the finite element simulations accounting for matrix failure and delamination were in a good agreement with that of the experiments in terms of the failure sequence and patterns in addition to the magnitudes of the strain fields.
- 4) Simulations demonstrate that the delaminations initiate and grow in a complex three-dimensional pattern, in which secondary delaminations are triggered by micro-cracks. After the end of the event, the delaminations merge into one major delaminated area on the top interface.
- 5) In the simulations, two element sizes are used and the global responses are found to be very similar. However, there are differences in the predictions of matrix crack distributions and total delaminated areas for different element

dimensions. The fine mesh, where each layer is modeled with two elements, resulted in a better agreement with experiments.

- 6) Similar to the element size effect, creating symmetric model and asymmetric meshing are also found to have considerable effect on the damage predictions. Although the major $350 \mu\text{s}$ delay between left and right hand cracks observed in the experiments could not be replicated, asymmetric meshing are found to create a similar sequential behavior.
- 7) Experimental scatter in the location and initiation time of first major matrix crack were accounted by statistically small variations in the material properties and the dynamic translation of stress fields as demonstrated by the finite element simulations.

In this thesis, the detailed experimental sequence and patterns of impact failure is presented. The experimental observations can also be taken as benchmark test cases, and they can be used in the validation of future composite damage models through low-velocity impact simulations.

As a complimentary future work to this study, conducting the same experimental and numerical work under quasi-static loading is planned for understanding the extent of wave propagation and its effects on the results of this study. In the experimental part, standard 3-point bending test fixture can be used with modifications to the load application head and the boundary conditions. For the simulations, the user-written VUMAT code will be modified into an ABAQUS/Standard UMAT subroutine to carry out static analyses.

REFERENCES

- [1] Roeseler WG, Sarh B, Kismarton M. Composite Structures-The First 100 Years. 16th Int. Conf. Compos. Mater., Kyoto, Japan: 2007.
- [2] ASM Material Data Sheet. asm.matweb.com (accessed December 21, 2015).
- [3] Niu M. Composite Airframe Structures Third Edition. Hong Kong Connilit Press Ltd 2010.
- [4] Choi HY, Wu H-YT, Chang F-K. A New Approach toward Understanding Damage Mechanisms and Mechanics of Laminated Composites Due to Low-Velocity Impact: Part II—Analysis. *J Compos Mater* 1991;25:1012–38.
- [5] Choi HY, Downs RJ, Chang F-K. A New Approach toward Understanding Damage Mechanisms and Mechanics of Laminated Composites Due to Low-Velocity Impact: Part I--Experiments. *J Compos Mater* 1991;25:992–1011.
- [6] Liu D. Impact-Induced Delamination--A View of Bending Stiffness Mismatching. *J Compos Mater* 1988;22:674–92.
- [7] Cantwell WJ, Morton J. Geometrical effects in the low velocity impact response of CFRP. *Compos Struct* 1989;12:39–59.
- [8] Abrate S. Impact on Laminated Composite Materials. *Appl Mech Rev* 1991;44:155.
- [9] Kim SJ, Goo NS, Kim TW. The effect of curvature on the dynamic response and impact-induced damage in composite laminates. *Compos Sci Technol* 1997;57:763–73.
- [10] González E V., Maimí P, Camanho PP, Lopes CS, Blanco N. Effects of ply clustering in laminated composite plates under low-velocity impact loading. *Compos Sci Technol* 2011;71:805–17.
- [11] Cantwell WJ, Morton J. Comparison of the low and high velocity impact response of CFRP. *Composites* 1989;20:545–51.
- [12] Rydin RW, Bushman MB, Karbhari VM. The Influence of Velocity in Low-Velocity Impact Testing of Composites Using the Drop Weight Impact Tower.

- J Reinf Plast Compos 1995;14:113–27.
- [13] Dost EF, Ilcewicz LB, Averyu WB, Coxon BR. Effects of Stacking Sequence on Impact Damage Resistance and Residual Strength for Quasi-Isotropic Laminates. *Compos. Mater. Fatigue Fract.*, 1991, p. 476–500.
- [14] Cantwell WWJ, Morton J. The impact resistance of composite materials — a review. *Composites* 1991;22:347–62.
- [15] SAE. CMH-17 - Composite Materials Handbook Volume: 3. 2012.
- [16] Beheshty M, Harris B. Post-impact fatigue behaviour of CFRP and the growth of low-velocity impact damage during fatigue. *Proc. First Int. Conf. Fatigue Compos.*, Paris: 1997, p. 355–62.
- [17] Rechak S, Sun CT. Optimal Use of Adhesive Layers in Reducing Impact Damage in Composite Laminates. *Compos. Struct.* 4, vol. 9, Dordrecht: Springer Netherlands; 1987, p. 18–31.
- [18] Choi HY, Chang FK. A Model for Predicting Damage in Graphite/Epoxy Laminated Composites Resulting from Low-Velocity Point Impact. *J Compos Mater* 1992;26:2134–69.
- [19] Richardson MOW, Wisheart MJ. Review of low-velocity impact properties of composite materials. *Compos Part A Appl Sci Manuf* 1996;27:1123–33.
- [20] ASTM D7136 / D7136M - 12 Standard Test Method for Measuring the Damage Resistance of a Fiber Reinforced Polymer Matrix Composite to a Drop Weight Impact Event n.d. <http://www.astm.org/Standards/D7136.htm> (accessed December 27, 2014).
- [21] ASTM D7137 / D7137M - 12 Standard Test Method for Compressive Residual Strength Properties of Damaged Polymer Matrix Composite Plates n.d. <http://www.astm.org/Standards/D7137.htm> (accessed December 29, 2014).
- [22] Geubelle PH, Baylor JS. Impact-induced delamination of composites: a 2D simulation. *Compos Part B Eng* 1998;29:589–602.
- [23] González E V., Maimí P, Camanho PP, Turon a., Mayugo J a. Simulation of drop-weight impact and compression after impact tests on composite laminates. *Compos Struct* 2012;94:3364–78.

- [24] Lopes CS, Camanho PP, Gürdal Z, Maimí P, González EV. Low-velocity impact damage on dispersed stacking sequence laminates. Part II: Numerical simulations. *Compos Sci Technol* 2009;69:937–47.
- [25] Pinho ST, Dávila CG, Camanho PP, Iannucci L, Robinson P. Failure models and criteria for FRP under in-plane or three-dimensional stress states including shear non-linearity 2005.
- [26] Maimí P, Camanho PP, Mayugo J a., Dávila CG. A continuum damage model for composite laminates: Part II – Computational implementation and validation. *Mech Mater* 2007;39:909–19.
- [27] Turon A., Camanho PP, Costa J, Dávila CG. A damage model for the simulation of delamination in advanced composites under variable-mode loading. *Mech Mater* 2006;38:1072–89.
- [28] Shi Y, Pinna C, Soutis C. Modelling impact damage in composite laminates: A simulation of intra- and inter-laminar cracking. *Compos Struct* 2014;114:10–9.
- [29] Bouvet C, Castanié B, Bizeul M, Barrau J-J. Low velocity impact modelling in laminate composite panels with discrete interface elements. *Int J Solids Struct* 2009;46:2809–21.
- [30] Bouvet C, Rivallant S, Barrau JJ. Low velocity impact modeling in composite laminates capturing permanent indentation. *Compos Sci Technol* 2012;72:1977–88.
- [31] Puck a., Schürmann H. Failure analysis of FRP laminates by means of physically based phenomenological models. *Compos Sci Technol* 2002;62:1633–62.
- [32] Tsai SW, Wu EM. A General Theory of Strength for Anisotropic Materials. *J Compos Mater* 1971;5:58–80.
- [33] Talreja R. Assessment of the fundamentals of failure theories for composite materials. *Compos Sci Technol* 2014;105:190–201.
- [34] Takeda N, Sierakowski RL, Ross C a., Malvern LE. Delamination-crack propagation in ballistically impacted glass/epoxy composite laminates. *Exp Mech* 1982;22:19–25.

- [35] Xu LR, Rosakis AJ. Impact Damage Visualization of Heterogeneous Two-layer Materials Subjected to Low-speed Impact. *Int J Damage Mech* 2005;14:215–33.
- [36] Camanho P, Dávilla CG. Mixed-Mode Decohesion Finite Elements in for the Simulation Composite of Delamination Materials. NASA 2002;TM-2002-21:1–37.
- [37] Simulia. ABAQUS 6.12-2 - Analysis User Manual. n.d.
- [38] Soden PD, Kaddour a. S, Hinton MJ. Recommendations for designers and researchers resulting from the world-wide failure exercise. *Compos Sci Technol* 2004;64:589–604.
- [39] Hashin Z. Failure Criteria for Unidirectional Fiber Composites. *J Appl Mech* 1980;47:329.
- [40] Dvorak GJ, Laws N. Analysis of Progressive Matrix Cracking In Composite Laminates II. First Ply Failure. *J Compos Mater* 1987;21:309–29.
- [41] Parvizi A, Garrett KW, Bailey JE. Constrained cracking in glass fibre-reinforced epoxy cross-ply laminates. *J Mater Sci* 1978;13:195–201.
- [42] Laws N. A note on interaction energies associated with cracks in anisotropic solids. *Philos Mag* 1977;36:367–72.
- [43] Wang ASD. Fracture Mechanics of Sublaminar Cracks in Composite Materials. *J Compos Technol Res* 1984;6:45.
- [44] Matzenmiller A, Lubliner J, Taylor RL. A constitutive model for anisotropic damage in fiber-composites. *Mech Mater* 1995;20:125–52.
- [45] English SA. A 3D Orthotropic Strain-Rate Dependent Elastic Damage Material Model. Livermore, California: 2014.
- [46] ASTM. ASTM Standard D6415. Standard Test Method for Measuring the Curved Beam Strength of a Fiber-Reinforced. West Conshohocken PA: 2006.
- [47] ASTM. ASTM Standard D2344. Standard Test Method for Short-Beam

Strength of Polymer Matrix Composite Materials. West Conshohocken PA: 2006.

- [48] Gözlüklü B. Modelling of Intersonic Delamination in Curved-Thick Composite Laminates under Quasi-Static Loading. Middle East Technical University, 2014.
- [49] ASTM International. Standard D5528. Standard Test Method for Mode I Interlaminar Fracture Toughness of Unidirectional Fiber-Reinforced Polymer Matrix Composites. West Conshohocken, PA, USA: 2013.
- [50] ASTM. ASTM Standard WK22949. New Test Method for Determination of the Mode II Interlaminar Fracture Toughness of Unidirectional Fiber-Reinforced Polymer Matrix Composites Using the End-Notched Flexure (ENF) Test. West Conshohocken PA: n.d.
- [51] Benzeggagh ML, Kenane M. Measurement of mixed-mode delamination fracture toughness of unidirectional glass/epoxy composites with mixed-mode bending apparatus. *Compos Sci Technol* 1996;56:439–49.
- [52] ASTM International. Standard D6671. Standard Test Method for Mixed Mode I-Mode II Interlaminar Fracture Toughness of. West Conshohocken PA: 2006.
- [53] ASTM International. Standard D3039. Standard test method for tensile properties of polymer matrix composite materials. West Conshohocken, PA, USA: 2000.
- [54] ASTM International. Standard D3410. Standard Test Method for Compressive Properties of Polymer Matrix Composite Materials with Unsupported Gage Section by Shear (D3410). West Conshohocken, PA, USA: 2008.
- [55] ASTM International. Standard D3518. Standard Test Method for In-Plane Shear Response of Polymer Matrix Composite Materials by Tensile Test of a ± 45 Laminate (D3518). West Conshohocken, PA, USA: 2013.
- [56] EN 2563. Determination of the apparent interlaminar shear strength of Carbon fibre reinforced plastics. 1997.
- [57] Martin R, Elms T, Bowron S. Characterisation of Mode II delamination using the 4 ENF. 4th Eur Conf Compos Test 1998.

- [58] Meng M, Le HR, Rizvi MJ, Grove SM. 3D FEA modelling of laminated composites in bending and their failure mechanisms. *Compos Struct* 2015;119:693–708.

APPENDIX

The following code is the VUMAT material subroutine used in the numerical simulations.

```
      subroutine vumat(
c Read only -
  1  nblock, ndir, nshr, nstatev, nfieldv, nprops, lanneal,
  2  stepTime, totalTime, dt, cmname, coordMp, charLength,
  3  props, density, strainInc, relSpinInc,
  4  tempOld, stretchOld, defgradOld, fieldOld,
  5  stressOld, stateOld, enerInternOld, enerInelasOld,
  6  tempNew, stretchNew, defgradNew, fieldNew,
c Write only -
  7  stressNew, stateNew, enerInternNew, enerInelasNew )
c
      include 'vaba_param.inc'
c
c 3D Orthotropic Elasticity with LaRC04 Failure criterion
c
c The state variables are stored as:
c   state(*,1) = material point status
c   state(*,2:7) = damping stresses
c
c User defined material properties are stored as
c * First line:
c   props(1) --> Young's modulus in 1-direction, E1
c   props(2) --> Young's modulus in 2-direction, E2
c   props(3) --> Young's modulus in 3-direction, E3
c   props(4) --> Poisson's ratio, nu12
c   props(5) --> Poisson's ratio, nu13
c   props(6) --> Poisson's ratio, nu23
c   props(7) --> Shear modulus, G12
c   props(8) --> Shear modulus, G13
c
c * Second line:
c   props(9) --> Shear modulus, G23
c   props(10) --> "not used"
c   props(11) --> "not used"
c   props(12) --> "not used"
c   props(13) --> "not used"
c   props(14) --> "not used"
c   props(15) --> "not used"
c   props(16) --> "not used"
c
c * Third line:
c   props(17) --> Ultimate tens stress in 1-direction, sigu1t
c   props(18) --> Ultimate comp stress in 1-direction, sigu1c
c   props(19) --> Ultimate tens stress in 2-direction, sigu2t
c   props(20) --> Ultimate comp stress in 2-direction, sigu2c
c   props(21) --> Ultimate tens stress in 3-direction, sigu3t
c   props(22) --> Ultimate comp stress in 3-direction, sigu3c
c   props(23) --> "not used"
c   props(24) --> "not used"
c
```

```

c * Fourth line:
c   props(25) --> Ultimate shear stress, sigu12
c   props(26) --> Ultimate shear stress, sigu13
c   props(27) --> Ultimate shear stress, sigu23
c   props(28) --> "not used"
c   props(29) --> "not used"
c   props(30) --> "not used"
c   props(31) --> "not used"
c   props(32) --> "not used"
c
    dimension props(nprops), density(nblock),
1   coordMp(nblock,*),
2   charLength(nblock), strainInc(nblock,ndir+nshr),
3   relSpinInc(nblock,nshr), tempOld(nblock),
4   stretchOld(nblock,ndir+nshr), defgradOld(nblock,ndir+nshr+nshr),
5   fieldOld(nblock,nfieldv), stressOld(nblock,ndir+nshr),
6   stateOld(nblock,nstatev), enerInternOld(nblock),
7   enerInelasOld(nblock), tempNew(*),
8   stretchNew(nblock,ndir+nshr), defgradNew(nblock,ndir+nshr+nshr),
9   fieldNew(nblock,nfieldv), stressNew(nblock,ndir+nshr),
1  stateNew(nblock,nstatev),
2  enerInternNew(nblock), enerInelasNew(nblock)
*
    character*80 cmname
*
    parameter( zero = 0.d0, one = 1.d0, two = 2.d0, half = .5d0 )
*
    parameter(
*       i_svd_DmgFiberT   = 1,
*       i_svd_DmgFiberC   = 2,
*       i_svd_DmgMatrixT  = 3,
*       i_svd_DmgMatrixC  = 4,
*       i_svd_statusMp    = 5,
*       i_svd_xdeq0t      = 6,
*       i_svd_xdeqft      = 7,
*       i_svd_xseq0t      = 8,
*       i_svd_xdeqtt      = 9,
*       i_svd_rmc         = 10,
*       i_svd_rmt         = 11,
*       i_svd_Strain      = 12,
c     *   i_svd_StrainXx   = 12,
c     *   i_svd_StrainYy   = 13,
c     *   i_svd_StrainZz   = 14,
c     *   i_svd_StrainXy   = 15,
c     *   i_svd_StrainYz   = 16,
c     *   i_svd_StrainZx   = 17,
*       i_svd_xdeq0c      = 18,
*       i_svd_xdeqfc      = 19,
*       i_svd_xseq0c      = 20,
*       i_svd_xdeqcc      = 21,
*       n_svd_required    = 21 )
*
    parameter(
*       i_s33_Xx = 1,
*       i_s33_Yy = 2,
*       i_s33_Zz = 3,
*       i_s33_Xy = 4,

```

```

*      i_s33_Yz = 5,
*      i_s33_Zx = 6 )
*
* Structure of property array
  parameter (
*      i_pro_E1      = 1,
*      i_pro_E2      = 2,
*      i_pro_E3      = 3,
*      i_pro_nu12    = 4,
*      i_pro_nu13    = 5,
*      i_pro_nu23    = 6,
*      i_pro_G12     = 7,
*      i_pro_G13     = 8,
*      i_pro_G23     = 9,
*
*      i_pro_beta    = 10,
*      i_pro_ER      = 11,
*
*      i_pro_sigu1t  = 17,
*      i_pro_sigu1c  = 18,
*      i_pro_sigu2t  = 19,
*      i_pro_sigu2c  = 20,
*      i_pro_sigu3t  = 21,
*      i_pro_sigu3c  = 22,
*      i_pro_sigu12  = 25,
*      i_pro_sigu13  = 26,
*      i_pro_sigu23  = 27 )

* Read material properties
*
  E1 = props(i_pro_E1)
  E2 = props(i_pro_E2)
  E3 = props(i_pro_E3)
  xnu12 = props(i_pro_nu12)
  xnu13 = props(i_pro_nu13)
  xnu23 = props(i_pro_nu23)
  G12 = props(i_pro_G12)
  G13 = props(i_pro_G13)
  G23 = props(i_pro_G23)
  ER = props(i_pro_ER)
*
  xnu21 = xnu12 * E2 / E1
  xnu31 = xnu13 * E3 / E1
  xnu32 = xnu23 * E3 / E2
*
*
* Compute terms of stiffness matrix
  gg = one / ( one - xnu12*xnu21 - xnu23*xnu32 - xnu31*xnu13
*      - two*xnu21*xnu32*xnu13 )
  C11 = E1 * ( one - xnu23*xnu32 ) * gg
  C22 = E2 * ( one - xnu13*xnu31 ) * gg
  C33 = E3 * ( one - xnu12*xnu21 ) * gg
  C12 = E1 * ( xnu21 + xnu31*xnu23 ) * gg
  C13 = E1 * ( xnu31 + xnu21*xnu32 ) * gg
  C23 = E2 * ( xnu32 + xnu12*xnu31 ) * gg
*
  f1t = props(i_pro_sigu1t)
  f1c = props(i_pro_sigu1c)

```

```

f2t = props(i_pro_sigu2t)
f2c = props(i_pro_sigu2c)
f3t = props(i_pro_sigu3t)
f3c = props(i_pro_sigu3c)
f12 = props(i_pro_sigu12)
f13 = props(i_pro_sigu13)
f23 = props(i_pro_sigu23)
*
    beta = props(i_pro_beta)
*
* Assume purely elastic material at the beginning of the analysis
*
*
    if ( totalTime .eq. zero ) then
        if (nstatev .lt. n_svd_Required) then
            call xplb_abqerr(-2,'Subroutine VUMAT requires the '//
                'specification of %I state variables. Check the '//
                'definition of *DEPVAR in the input file.',
                n_svd_Required,zero,' ')
            call xplb_exit
        end if
        call OrthoEla3dExp ( nblock,
            *   stateOld(1,i_svd_DmgFiberT),
            *   stateOld(1,i_svd_DmgFiberC),
            *   stateOld(1,i_svd_DmgMatrixT),
            *   stateOld(1,i_svd_DmgMatrixC),
            *   E1,E2,E3,xnu12,xnu21,xnu13,xnu31,xnu23,xnu32, G12,G23,G13,
            *   strainInc, stressNew)
        return
    end if
*
* Update total elastic strain
    call strainUpdate ( nblock, strainInc,
        *   stateOld(1,i_svd_strain), stateNew(1,i_svd_strain) )
*
* Stress update
    call OrthoEla3dExp ( nblock,
        *   stateOld(1,i_svd_DmgFiberT),
        *   stateOld(1,i_svd_DmgFiberC),
        *   stateOld(1,i_svd_DmgMatrixT),
        *   stateOld(1,i_svd_DmgMatrixC),
        *   E1,E2,E3,xnu12,xnu21,xnu13,xnu31,xnu23,xnu32, G12,G23,G13,
        *   stateNew(1,i_svd_strain),
        *   stressNew)
*
* Failure evaluation
*
    call copyr ( nblock,
        *   stateOld(1,i_svd_DmgFiberT), stateNew(1,i_svd_DmgFiberT) )
    call copyr ( nblock,
        *   stateOld(1,i_svd_DmgFiberC), stateNew(1,i_svd_DmgFiberC) )
    call copyr ( nblock,
        *   stateOld(1,i_svd_DmgMatrixT), stateNew(1,i_svd_DmgMatrixT) )
    call copyr ( nblock,
        *   stateOld(1,i_svd_DmgMatrixC), stateNew(1,i_svd_DmgMatrixC) )
    call copyr ( nblock,
        *   stateOld(1,i_svd_xdeq0t), stateNew(1,i_svd_xdeq0t) )
    call copyr ( nblock,

```

```

*   stateOld(1,i_svd_xdeqft), stateNew(1,i_svd_xdeqft) )
call copyr ( nblock,
*   stateOld(1,i_svd_xseq0t), stateNew(1,i_svd_xseq0t) )
call copyr ( nblock,
*   stateOld(1,i_svd_xdeqtt), stateNew(1,i_svd_xdeqtt) )
call copyr ( nblock,
*   stateOld(1,i_svd_xdeq0c), stateNew(1,i_svd_xdeq0c) )
call copyr ( nblock,
*   stateOld(1,i_svd_xdeqfc), stateNew(1,i_svd_xdeqfc) )
call copyr ( nblock,
*   stateOld(1,i_svd_xseq0c), stateNew(1,i_svd_xseq0c) )
call copyr ( nblock,
*   stateOld(1,i_svd_xdeqcc), stateNew(1,i_svd_xdeqcc) )
nDmg = 0
call LaRC04 ( nblock, nDmg, charLength,
*   f1t, f2t, f3t, f1c, f2c, f3c, f12, f23, f13, G12,
*   E1, E2, xnu21,
*   stateNew(1,i_svd_DmgFiberT),
*   stateNew(1,i_svd_DmgFiberC),
*   stateNew(1,i_svd_DmgMatrixT),
*   stateNew(1,i_svd_rmt),
*   stateNew(1,i_svd_DmgMatrixC),
*   stateNew(1,i_svd_rmc),
*   stateNew(1,i_svd_statusMp),
*   stressNew, stateNew(1,i_svd_strain),
*   ER,
*   stateNew(1,i_svd_xdeq0t),
*   stateNew(1,i_svd_xdeq0c),
*   stateNew(1,i_svd_xdeqft),
*   stateNew(1,i_svd_xdeqfc),
*   stateNew(1,i_svd_xseq0t),
*   stateNew(1,i_svd_xseq0c),
*   stateNew(1,i_svd_xdeqtt),
*   stateNew(1,i_svd_xdeqcc))
*
*   -- Recompute stresses if new Damage is occurring
if ( nDmg .gt. 0 ) then
  call OrthoEla3dExp ( nblock,
*   stateNew(1,i_svd_DmgFiberT),
*   stateNew(1,i_svd_DmgFiberC),
*   stateNew(1,i_svd_DmgMatrixT),
*   stateNew(1,i_svd_DmgMatrixC),
*   E1,E2,E3,xnu12,xnu21,xnu13,xnu31,xnu23,xnu32, G12,G23,G13,
*   stateNew(1,i_svd_strain),
*   stressNew)
  end if
*
* Integrate the internal specific energy (per unit mass)
*
  call EnergyInternal3d ( nblock, stressOld, stressNew,
*   strainInc, density, enerInternOld, enerInternNew,
*   stateNew(1,i_svd_DmgMatrixT))
*
* Integrate the specific strain energy (per unit mass)
*(Inelastic energy variable is used)
*
  call EnergyStrain (nblock, stateNew(1,i_svd_strain),
*   stressNew, density, enerInelasOld, enerInelasNew)

```

```

*
    return
end

*****
*   OrthoEla3dExp: Orthotropic elasticity - 3d   *
*****
    subroutine OrthoEla3dExp ( nblock,
*       dmgFiberT, dmgFiberC, dmgMatrixT, dmgMatrixC,
*       E1,E2,E3,xnu12,xnu21,xnu13,xnu31,xnu23,xnu32, G12, G23, G13,
*       strain, stress)
*
    include 'vaba_param.inc'

*   Orthotropic elasticity, 3D case -
*
    parameter( zero = 0.d0, one = 1.d0, two = 2.d0, zeroone = 0.1d0)
    parameter(
*       i_s33_Xx = 1,
*       i_s33_Yy = 2,
*       i_s33_Zz = 3,
*       i_s33_Xy = 4,
*       i_s33_Yz = 5,
*       i_s33_Zx = 6,
*       n_s33_Car = 6 )
*
    dimension strain(nblock,n_s33_Car),
*       dmgFiberT(nblock), dmgFiberC(nblock),
*       dmgMatrixT(nblock), dmgMatrixC(nblock),
*       stress(nblock,n_s33_Car),
*       xdeq0(nblock), xdeqf(nblock),
*       xseq0(nblock), xdeq (nblock),
*       xdeqInv(nblock), xdeqf0 (nblock),
*       xdeqf0Inv(nblock)

*   -- shear fraction in matrix tension and compression mode
    parameter ( smt = 0.9d0, smc = 0.5d0 )
*
    do k = 1, nblock
*   -- Compute damaged stiffness
        dft = dmgFiberT(k)
        dfc = dmgFiberC(k)
        dmt = dmgMatrixT(k) * 0.99d0
        dmc = dmgMatrixC(k) * 0.99d0
        df = one - ( one - dft ) * ( one - dfc )
        s22 = stress(k,i_s33_Yy)
        s33 = stress(k,i_s33_Zz)
        if ((s22+s33) .ge. zero) then
            dm = dmt
        else
            dm = dmc
        endif
        ds = one - (one-dft)*(one-dfc)*(one-dmt)*(one-dmc)
*
        dC11 = -(- E1*xnu23*xnu32*dm**2 +two*E1*xnu23*xnu32*dm + E1-E1
*       *xnu23*xnu32)/(xnu12*xnu21 + xnu13*xnu31 + xnu23*xnu32 +
*       dm**2*xnu23*xnu32 - dm*xnu12*xnu21 - dm*xnu13*xnu31 - two*dm*
*       xnu23*xnu32 + xnu12*xnu23*xnu31 + xnu13*xnu21*xnu32 - two*dm*

```

```

* xnu12*xnu23*xnu31 - two*dm*xnu13*xnu21*xnu32+dm**2*xnu12*xnu23*
* xnu31 +dm**2*xnu13*xnu21*xnu32 - one)
dC22 = ((dm - one)*(E2 - E2*xnu13*xnu31 + E2*dm*xnu13*xnu31))/
* (xnu12*xnu21 + xnu13*xnu31 + xnu23*xnu32 + dm**2*xnu23*xnu32 -
* dm*xnu12*xnu21 - dm*xnu13*xnu31 - two*dm*xnu23*xnu32 + xnu12*
* xnu23*xnu31 + xnu13*xnu21*xnu32 - two*dm*xnu12*xnu23*xnu31 -
* two*dm*xnu13*xnu21*xnu32 + dm**2*xnu12*xnu23*xnu31+dm**2*xnu13*
* xnu21*xnu32 - one)
dC33 = ((dm - one)*(E3 - E3*xnu12*xnu21 + E3*dm*xnu12*xnu21))/
* (xnu12*xnu21 + xnu13*xnu31 + xnu23*xnu32 + dm**2*xnu23*xnu32 -
* dm*xnu12*xnu21 - dm*xnu13*xnu31 - two*dm*xnu23*xnu32 +
* xnu12*xnu23*xnu31 + xnu13*xnu21*xnu32 - two*dm*xnu12*xnu23*
* xnu31 - two*dm*xnu13*xnu21*xnu32+dm**2*xnu12*xnu23*xnu31+dm**2*
* xnu13*xnu21*xnu32 - one)
dC12 = ((dm - one)*(E1*xnu21 + E1*xnu23*xnu31 - E1*dm*xnu23*
* xnu31))/(xnu12*xnu21 + xnu13*xnu31 + xnu23*xnu32 + dm**2*xnu23*
* xnu32 - dm*xnu12*xnu21 - dm*xnu13*xnu31 - two*dm*xnu23*xnu32 +
* xnu12*xnu23*xnu31 + xnu13*xnu21*xnu32-two*dm*xnu12*xnu23*xnu31
* - two*dm*xnu13*xnu21*xnu32 + dm**2*xnu12*xnu23*xnu31 + dm**2*
* xnu13*xnu21*xnu32 - one)
dC21 = -(E2*xnu12 - E2*dm*xnu12 + E2*xnu13*xnu32 + E2*dm**2*
* xnu13*xnu32 - two*E2*dm*xnu13*xnu32)/(xnu12*xnu21+ xnu13*xnu31+
* xnu23*xnu32 + dm**2*xnu23*xnu32 - dm*xnu12*xnu21 - dm*xnu13*
* xnu31 - two*dm*xnu23*xnu32 + xnu12*xnu23*xnu31 + xnu13*xnu21*
* xnu32 -two*dm*xnu12*xnu23*xnu31-two*dm*xnu13*xnu21*xnu32+dm**2*
* xnu12*xnu23*xnu31 + dm**2*xnu13*xnu21*xnu32 - one)
dC23 = ((dm - one)*(E2*xnu32 - E2*dm*xnu32 + E2*xnu12*xnu31 -
* E2*dm*xnu12*xnu31))/(xnu12*xnu21 + xnu13*xnu31 + xnu23*xnu32 +
* dm**2*xnu23*xnu32 - dm*xnu12*xnu21 - dm*xnu13*xnu31 - two*dm*
* xnu23*xnu32 + xnu12*xnu23*xnu31+xnu13*xnu21*xnu32-two*dm*xnu12*
* xnu23*xnu31 - two*dm*xnu13*xnu21*xnu32+dm**2*xnu12*xnu23*xnu31+
* dm**2*xnu13*xnu21*xnu32 - one)
dC32 = ((dm - one)*(E3*xnu23 - E3*dm*xnu23 + E3*xnu13*xnu21-E3*
* dm*xnu13*xnu21))/(xnu12*xnu21 + xnu13*xnu31 + xnu23*xnu32 +
* dm**2*xnu23*xnu32 - dm*xnu12*xnu21 - dm*xnu13*xnu31 - two*dm*
* xnu23*xnu32 + xnu12*xnu23*xnu31 + xnu13*xnu21*xnu32 -
* two*dm*xnu12*xnu23*xnu31- two*dm*xnu13*xnu21*xnu32+dm**2*xnu12*
* xnu23*xnu31 + dm**2*xnu13*xnu21*xnu32 - one)
dC13 = ((dm - one)*(E1*xnu31 + E1*xnu21*xnu32 - E1*dm*xnu21*
* xnu32))/(xnu12*xnu21 + xnu13*xnu31 + xnu23*xnu32 + dm**2*xnu23*
* xnu32 - dm*xnu12*xnu21 - dm*xnu13*xnu31 - two*dm*xnu23*xnu32 +
* xnu12*xnu23*xnu31 + xnu13*xnu21*xnu32 -two*dm*xnu12*xnu23*xnu31
* - two*dm*xnu13*xnu21*xnu32 + dm**2*xnu12*xnu23*xnu31 + dm**2*
* xnu13*xnu21*xnu32 - one)
dC31 = -(E3*xnu13 - E3*dm*xnu13 + E3*xnu12*xnu23 + E3*dm**2*
* xnu12*xnu23 - two*E3*dm*xnu12*xnu23)/(xnu12*xnu21 +xnu13*xnu31+
* xnu23*xnu32 + dm**2*xnu23*xnu32 - dm*xnu12*xnu21 - dm*xnu13*
* xnu31 - two*dm*xnu23*xnu32 + xnu12*xnu23*xnu31 + xnu13*xnu21*
* xnu32 -two*dm*xnu12*xnu23*xnu31-two*dm*xnu13*xnu21*xnu32+dm**2*
* xnu12*xnu23*xnu31 + dm**2*xnu13*xnu21*xnu32 - one)
dC44 = -2.d0*G12*(ds - one)
dC55 = -2.d0*G13*(ds - one)
dC66 = -2.d0*G23*(ds - one)
* -- Stress update
stress(k,i_s33_Xx) = dC11 * strain(k,i_s33_Xx)
* + dC12 * strain(k,i_s33_Yy)
* + dC13 * strain(k,i_s33_Zz)
stress(k,i_s33_Yy) = dC21 * strain(k,i_s33_Xx)

```

```

*      + dC22 * strain(k,i_s33_Yy)
*      + dC23 * strain(k,i_s33_Zz)
stress(k,i_s33_Zz) = dC31 * strain(k,i_s33_Xx)
*      + dC32 * strain(k,i_s33_Yy)
*      + dC33 * strain(k,i_s33_Zz)
stress(k,i_s33_Xy) = dC44 * strain(k,i_s33_Xy)
stress(k,i_s33_Yz) = dC55 * strain(k,i_s33_Yz)
stress(k,i_s33_Zx) = dC66 * strain(k,i_s33_Zx)
end do
*
return
end

*****
* strainUpdate: Update total strain *
*****
subroutine strainUpdate ( nblock,
*      strainInc, strainOld, strainNew )
*
include 'vaba_param.inc'
*
parameter(
*      i_s33_Xx = 1,
*      i_s33_Yy = 2,
*      i_s33_Zz = 3,
*      i_s33_Xy = 4,
*      i_s33_Yz = 5,
*      i_s33_Zx = 6,
*      n_s33_Car = 6 )
*
dimension strainInc(nblock,n_s33_Car),
*      strainOld(nblock,n_s33_Car),
*      strainNew(nblock,n_s33_Car)
*
do k = 1, nblock
strainNew(k,i_s33_Xx)= strainOld(k,i_s33_Xx)
*      + strainInc(k,i_s33_Xx)
strainNew(k,i_s33_Yy)= strainOld(k,i_s33_Yy)
*      + strainInc(k,i_s33_Yy)
strainNew(k,i_s33_Zz)= strainOld(k,i_s33_Zz)
*      + strainInc(k,i_s33_Zz)
strainNew(k,i_s33_Xy)= strainOld(k,i_s33_Xy)
*      + strainInc(k,i_s33_Xy)
strainNew(k,i_s33_Yz)= strainOld(k,i_s33_Yz)
*      + strainInc(k,i_s33_Yz)
strainNew(k,i_s33_Zx)= strainOld(k,i_s33_Zx)
*      + strainInc(k,i_s33_Zx)
end do
*
return
end

*****
* LaRC04 criterion: Evaluate 3d Matrix failure *
*****
subroutine LaRC04 ( nblock, nDmg, charLength,
*      f1t, f2t, f3t, f1c, f2c, f3c, f12, f23, f13, G12,

```

```

*      E1, E2, xnu21,
*      dmgFiberT, dmgFiberC, dmgMatrixT, rmt, dmgMatrixC, rmc,
*      statusMp, stress, strain, ER, xdeq0t, xdeq0c, xdeqft,
*      xdeqfc, xseq0t, xseq0c, xdeqtt, xdeqcc)
*
*      include 'vaba_param.inc'
*      real*8 a22, a23
*
*      parameter( zero = 0.d0, one = 1.d0, two = 2.d0, three = 3.d0 )
*      parameter(
*          i_s33_Xx = 1,
*          i_s33_Yy = 2,
*          i_s33_Zz = 3,
*          i_s33_Xy = 4,
*          i_s33_Yz = 5,
*          i_s33_Zx = 6,
*          n_s33_Car = 6 )
*
*      parameter(i_v3d_X=1,i_v3d_Y=2,i_v3d_Z=3 )
*      parameter(n_v3d_Car=3 )
*      parameter (xa0 = 0.9250245)
*
*      parameter ( eMax = 5.99d0, eMin = -0.8d0 )
*
*      dimension charLength (nblock), xdeq0t (nblock),xdeq0c (nblock),
*      dmgFiberT(nblock), dmgFiberC(nblock),
*      dmgMatrixT(nblock), rmt(nblock), dmgMatrixC(nblock),
*      rmc(nblock), stress(nblock,n_s33_Car),
*      statusMp(nblock),
*      strain(nblock,n_s33_Car),
*      xdeqft (nblock), xdeqfc (nblock), xseq0t (nblock),
*      xseq0c (nblock), xdeqt (nblock), xdeqc (nblock),
*      xdeqttInv(nblock), xdeqccInv(nblock), xdeqf0t (nblock),
*      xdeqf0c (nblock), xdeqf0tInv(nblock), xdeqf0cInv(nblock),
*      xdeqtt (nblock), xdeqcc (nblock)
*
*      f1tInv = zero
*      f2tInv = zero
*      f3tInv = zero
*      f1cInv = zero
*      f2cInv = zero
*      f3cInv = zero
*      f12Inv = zero
*      f23Inv = zero
*      f13Inv = zero
*
*      if ( f1t .gt. zero ) f1tInv = one / f1t
*      if ( f2t .gt. zero ) f2tInv = one / f2t
*      if ( f3t .gt. zero ) f3tInv = one / f3t
*      if ( f1c .gt. zero ) f1cInv = one / f1c
*      if ( f2c .gt. zero ) f2cInv = one / f2c
*      if ( f3c .gt. zero ) f3cInv = one / f3c
*      if ( f12 .gt. zero ) f12Inv = one / f12
*      if ( f23 .gt. zero ) f23Inv = one / f23
*      if ( f13 .gt. zero ) f13Inv = one / f13
*
*      do k = 1, nblock
*          if ( statusMp(k) .eq. one ) then

```

```

*
    lFail = 0
*
    s11 = stress(k,i_s33_Xx)
    s22 = stress(k,i_s33_Yy)
    s33 = stress(k,i_s33_Zz)
    s12 = stress(k,i_s33_Xy)
    s23 = stress(k,i_s33_Yz)
    s13 = stress(k,i_s33_Zx)
    xe12 = strain(k,i_s33_Xy)
    xe22 = strain(k,i_s33_Yy)
    xe13 = strain(k,i_s33_Xy)
    xe23 = strain(k,i_s33_Yz)
    xe33 = strain(k,i_s33_Zz)
    charL = charLength(k)
*
*   Evaluate Fiber modes
*   if ( s11 .gt. zero ) then
*   -- Tensile Fiber Mode
*****
*   -- Compressive Fiber Mode
*****
*   Evaluate Matrix Modes
*   -- Tensile Matrix Mode
*
    a22 = two * (one / E2 - xnu21**2 / E1)
    a23 = a22
    uy12 = f12/G12
    xuy12 = G12 * uy12**2
    uy12is = (two * xuy12 / G12)**0.5
    xuy12is = G12 * uy12is**2
    xy12 = G12 * xe12**2
    ytis = 1.12d0 * two**0.5 * f2t
    xg = 1.12d0**2 * (a22 * f2t**2 / xuy12)
*
    if ( ( s22 ) .gt. zero) then
*
        rmt (k) = ( one - xg ) * (s22 / ytis)
*           + xg * ( (s22 / ytis)**2 )
*           + (( a23 * s23**2 + xy12 ) / (xuy12is))
*
        if (( rmt(k) .ge. one ) .or. (dmgMatrixT(k) .gt. zero)) then
            lDmg = 1
            xdeqt (k) = charL * (((xe33 + abs(xe33))/two) **2 +
*                ((xe22 + abs(xe22))/two) + xe23**2 +
*                xe13**2 + xe12**2) **0.5
            if (xdeqt (k) .gt. xdeqtt (k)) xdeqtt(k) = xdeqt(k)
            if ( xdeq0t (k) .eq. zero ) then
                xdeq0t (k) = charL * (((xe33 + abs(xe33))/two)**2 +
*                ((xe22 + abs(xe22))/two) + xe23**2 +
*                xe13**2 + xe12**2) **0.5
                xseq0t (k) = ((s33 + abs(s33))/two *
*                (xe33 + abs(xe33)) / two + (s22 + abs(s22))/
*                two * (xe22 + abs(xe22)) / two + s12*xe12 +
*                s13*xe13 + s23 * xe23) /
*                (xdeq0t (k) / charL)
                xdeqft (k) = (two * ER / xseq0t (k))
            end if

```

```

xdef0t (k) = xdef0t(k) - xdef0t(k)
if ( xdef0t(k) .gt. zero ) then
  xdef0tInv (k) = one / xdef0t(k)
end if
if ( xdef0t (k) .gt. zero ) then
  xdef0tInv (k) = one / xdef0t(k)
end if
dmgMatrixT(k) = xdef0t(k) * (xdef0t(k) - xdef0t(k)) *
*   xdef0tInv (k) * xdef0tInv (k)
if (dmgMatrixT(k) .gt. one) dmgMatrixT(k) = one
if (dmgMatrixT(k) .lt. zero) dmgMatrixT(k) = zero
end if
else if ( ( s22) .lt. zero ) then
*
*   -- Compressive Matrix Mode
*
  xnt = -1.d0 / tan (2*xa0)
  Slis = sqrt(2.d0)*f12
  St = f2c * cos (xa0) * (sin (xa0) + cos(xa0) / tan(2*xa0))
  xnl = xnt * Slis / St
  xsn = (s22+s33)/2 + (s22-s33)/2*cos(2*xa0) + s23*sin(2*xa0)
  xtt = (s22+s33)/2 - (s22-s33)/2*sin(2*xa0) + s23*cos(2*xa0)
  xtl = s12*cos(xa0) + s13 * sin(xa0)
  rmc (k) = (xtt/(St-xnt*xsn))**2 +
*   (xtl/(Slis-xnl*xsn))**2
*
  if ( (rmc (k) .ge. one) .or. (dmgMatrixC(k) .gt. zero)) then
    lDmg = 1
    xdeqc (k) = charL * (((-xe33 + abs(-xe33))/two) **2 +
*   ((-xe22 + abs(-xe22))/two) + xe23**2 +
*   xe13**2 + xe12**2) **0.5
    if (xdeqc (k) .gt. xdeqcc (k)) xdeqcc(k) = xdeqc(k)
    if ( xdeq0c (k) .eq. zero ) then
      xdeq0c (k) = charL * (((-xe33 + abs(-xe33))/two)**2+
*   ((-xe22 + abs(-xe22))/two) + xe23**2 +
*   xe13**2 + xe12**2) **0.5
      xseq0c (k) = ((-s33 + abs(-s33))/two *
*   (-xe33 + abs(-xe33)) / two +(-s22 + abs(-s22))/
*   two * (-xe22 + abs(-xe22)) / two + s12*xe12 +
*   s13*xe13 + s23 * xe23) /
*   (xdeq0c (k) / charL)
      xdefc (k) = (two * ER / xseq0c (k))
    end if
    xdef0c (k) = xdefc(k) - xdef0c(k)
    if ( xdeqcc(k) .gt. zero ) then
      xdeqccInv (k) = one / xdeqcc(k)
    end if
    if ( xdef0c (k) .gt. zero ) then
      xdef0cInv (k) = one / xdef0c(k)
    end if
    dmgMatrixC(k) = xdefc(k) * (xdeqcc(k) - xdef0c(k)) *
*   xdeqccInv (k) * xdef0cInv (k)
    if (dmgMatrixC(k) .gt. one) dmgMatrixC(k) = one
    if (dmgMatrixC(k) .lt. zero) dmgMatrixC(k) = zero
  end if
end if
*
*

```

```

        if ( dmgFiberT(k) .eq. one ) then
            statusMp(k) = zero
        end if
*
        nDmg = nDmk + lDmg
*
        end if
*
    end do
*
    return
end
*
*****
*   EnergyInternal3d: Compute internal energy for 3d case   *
*****
        subroutine EnergyInternal3d(nblock, sigOld, sigNew ,
*   strainInc, curDensity, enerInternOld, enerInternNew,dmgMatrixT)
*
        include 'vaba_param.inc'
*
        parameter(
*   i_s33_Xx = 1,
*   i_s33_Yy = 2,
*   i_s33_Zz = 3,
*   i_s33_Xy = 4,
*   i_s33_Yz = 5,
*   i_s33_Zx = 6,
*   n_s33_Car = 6 )
*
        parameter( two = 2.d0, half = .5d0, zero = 0.d0 )
*
        dimension sigOld (nblock,n_s33_Car), sigNew (nblock,n_s33_Car),
*   strainInc (nblock,n_s33_Car), curDensity (nblock),
*   enerInternOld(nblock), enerInternNew(nblock),
*   dmgMatrixT(nblock)
*
        do k = 1, nblock
            stressPower = half * (
*   ( sigOld(k,i_s33_Xx) + sigNew(k,i_s33_Xx) )
*   * ( strainInc(k,i_s33_Xx) )
*   + ( sigOld(k,i_s33_Yy) + sigNew(k,i_s33_Yy) )
*   * ( strainInc(k,i_s33_Yy) )
*   + ( sigOld(k,i_s33_Zz) + sigNew(k,i_s33_Zz) )
*   * ( strainInc(k,i_s33_Zz) )
*   + two * ( sigOld(k,i_s33_Xy) + sigNew(k,i_s33_Xy) )
*   * strainInc(k,i_s33_Xy)
*   + two * ( sigOld(k,i_s33_Yz) + sigNew(k,i_s33_Yz) )
*   * strainInc(k,i_s33_Yz)
*   + two * ( sigOld(k,i_s33_Zx) + sigNew(k,i_s33_Zx) )
*   * strainInc(k,i_s33_Zx) )
*
            enerInternNew(k) =enerInternOld(k)+stressPower/curDensity(k)
        end do
*
        return
end
*****

```

```

* Calculate Specific Strain Energy (in ALLPD variable) *
*****
subroutine EnergyStrain(nblock, strain, sigNew, curDensity,
* enerInelasOld, enerInelasNew)
*
include 'vaba_param.inc'
*
parameter(
* i_s33_Xx = 1,
* i_s33_Yy = 2,
* i_s33_Zz = 3,
* i_s33_Xy = 4,
* i_s33_Yz = 5,
* i_s33_Zx = 6,
* n_s33_Car = 6 )
*
parameter( half = .5d0, two=2.d0)
*
dimension sigNew (nblock,n_s33_Car), strain (nblock,n_s33_Car),
* enerInelasOld (nblock), enerInelasNew(nblock),
* curDensity (nblock)
*
do k = 1, nblock
stresspowertwo = half * (
* ( sigNew(k,i_s33_Xx) ) * ( strain(k,i_s33_Xx))
* + ( sigNew(k,i_s33_Yy) ) * ( strain(k,i_s33_Yy))
* + ( sigNew(k,i_s33_Zz) ) * ( strain(k,i_s33_Zz))
* + two * ( sigNew(k,i_s33_Xy) ) * strain(k,i_s33_Xy)
* + two * ( sigNew(k,i_s33_Yz) ) * strain(k,i_s33_Yz)
* + two * ( sigNew(k,i_s33_Zx) ) * strain(k,i_s33_Zx) )
enerInelasNew (k) = stresspowertwo/curDensity(k)
enerInelasOld (k) = enerInelasNew (k)
end do
*
return
end

*****
* CopyR: Copy from one array to another *
*****
subroutine CopyR(nCopy, from, to )
*
include 'vaba_param.inc'
*
dimension from(nCopy), to(nCopy)
*
do k = 1, nCopy
to(k) = from(k)
end do
*
return
end

```